Aalto University
School of Engineering
Degree Programme in Mechanical Engineering

Matti Palin

Analysis of aerodynamic stability of the MetNet Entry and Descent vehicle with FINFLO simulations

Master's Thesis
Espoo, October 31, 2015

Supervisor: Professor Jukka Tuhkuri, Aalto University
Advisors: Professor Timo Siikonen
Ari-Matti Harri, D.Sc. (Tech.) (Finnish Meteorological Institute)

Aalto University
School of Engineering
Degree Programme in Mechanical Engineering

ABSTRACT OF
MASTER'S THESIS

Author: Matti Palin

Title:
Analysis of aerodynamic stability of the MetNet Entry and Descent vehicle with FINFLO simulations

Date: October 31, 2015 **Pages:** xiv + 86

Major: Aeronautical Engineering **Code:** K3004

Supervisor: Professor Jukka Tuhkuri

Advisors: Professor Timo Siikonen
Ari-Matti Harri, D.Sc. (Tech.) (Finnish Meteorological Institute)

This Master's Thesis investigates the aerodynamic stability of the MetNet Mars atmospheric entry and descent vehicle, developed in cooperation between the Finnish Meteorological Institute (FMI) and the Lavochin Association (LA). The purpose of the study is performing Computational Fluid Dynamics (CFD) simulations and obtaining the pertinent aerodynamic coefficients for the vehicle in the landing phase to Mars. The results are compared with the values obtained by LA, the most important feature being the aerodynamic stability of the vehicle. In this work, only the static stability is assessed.

The simulations were performed with an inhouse FINFLO software. Before the simulations, an atmospheric model of Mars was created. Some initial trajectory calculations were made in order to have approximate values for the combinations of the Reynolds and Mach numbers that the vehicle will experience during the landing. These initial trajectory calculations also provided a condition for the mesh creation. A coarse and a dense calculation meshes were created with 1.4 and 7 million cells, respectively. The SST k-ω turbulence model was used and the results were tabulated in a form of dimensionless coefficients.

Apart from the lift coefficient, the values differ to some extent from the LA's results. However, the general trends lead to the same conclusions: the drag coefficient is more than sufficient to ensure the designed landing speed and the negative slope of the pitching moment coefficient indicates static stability for the vehicle. Some heat load analyses were also carried out. Unfortunately, the simulations converged only up to Ma = 1.9 and no results were obtained at larger velocities. The thermal analyses show that heating of the vehicle is highly dependent on the Mach number, and for these reasons it would be advisable to perform more simulations for the vehicle.

Keywords: CFD, FINFLO, simulation, MetNet, Mars, lander, stability

Language: English

Aalto-yliopisto
Insinööritieteiden korkeakoulu
Konetekniikan koulutusohjelma

DIPLOMITYÖN
TIIVISTELMÄ

Tekijä:	Matti Palin		
Työn nimi:	MetNet-laskeutujan aerodynaamisen vakavuuden analysointi FINFLO-simulaatioilla		
Päiväys:	31. lokakuuta 2015	**Sivumäärä:**	xiv + 86
Pääaine:	Lentotekniikka	**Koodi:**	K3004
Valvoja:	Professori Jukka Tuhkuri		
Ohjaajat:	Professori Timo Siikonen Tekniikan tohtori Ari-Matti Harri (Ilmatieteen Laitos)		

Tässä diplomityössä tutkitaan Ilmatieteen Laitoksen ja Lavochin Associationin (LA) kehittämän Mars MetNet-laskeutujan aerodynaamista vakavuutta käyttäen laskennallista virtausmekaniikkaa. Tavoitteena on ratkaista relevantit aerodynaamiset kertoimet laskeutumisvaiheen aikana Marsiin. Tuloksia verrataan LA:n saamiin arvoihin ja tärkeimpänä tutkittavana ominaisuutena on aerodynaaminen vakavuus. Työssä tutkitaan vain staattista aerodynaamista stabiiliutta.

Laskentaan käytettiin FINFLO-ohjelmaa. Marsin kaasukehästä luotiin malli ennen simulaatioita. Lisäksi tehtiin ratalaskelmia laskeutujan laskeutumisvaiheen aikana kokemien Reynoldsin luvun ja Machin luvun arvojen saamiseksi. Ratalaskelmat tuottivat myös ehdon, joka auttoi laskentaverkon luomisessa. Laskentaa varten luotiin harva ja tiheä laskentaverkko, joissa oli 1,4 ja 7 miljoonaa laskentakoppia. Turbulenssin kuvaukseen käytettiin SST k-ω-mallia ja tulokset taulukoitiin dimensiottomassa kerroinmuodossa.

Nostovoimakerrointa lukuun ottamatta tulokset erosivat jonkin verran LA:n saamista arvoista. Tuloksista voidaan kuitenkin tehdä sama päätelmä: laskeutujan vastuskerroin on enemmän kuin riittävä suunniteltuun laskeutumisnopeuteen nähden ja pituusmomenttikertoimen negatiivinen kulmakerroin osoittaa laskeutujan olevan staattisesti stabiili. Laskenta ei kuitenkaan konvergoitunut suuremmilla Machin luvuilla kuin $\mathrm{Ma} = 1,9$ eikä tuloksia saatu tätä suuremmilla nopeuksilla. Lämpötarkastelut osoittivat lisäksi laskeutujan pintalämpötilan olevan voimakkaasti riippuvainen Machin luvusta ja näistä syistä laskeutujalle suositellaan suoritettavan lisää simulaatioita.

Asiasanat:	CFD, FINFLO, simulaatio, MetNet, Mars, laskeutuja, vakavuus
Kieli:	Englanti

Acknowledgements

This thesis was created between January and September 2015 at the Mechanical Engineering Department of the Aalto University in Otaniemi. This research was initiated and funded by the Finnish Meteorological Institute in order to answer their need for aerodynamic research for the MetNet lander.

I wish to thank first and foremost professor Timo Siikonen for giving me the great occasion to work on this project. I am thankful for all the support and guidance he has given me throughout the project. I am also grateful to my supervisor Jukka Tuhkuri for the possibility to carry out my research in the Department of Mechanical Engineering. Furthermore, I would like to thank Dr. Ari-Matti Harri and Harri Haukka for providing all the necessary material for the work and for help along the way. Moreover, I wish to thank Lucien Vienne (Université de Toulon) for his conducive observations and cooperation during his internship in the department.

My gratitude goes also to the Department and staff of Mechanical Engineering of the Aalto University for providing me with the necessary facilities, know-how, and hardware for the demanding project.

Espoo, October 31, 2015

Matti Palin

Abbreviations and Acronyms

CAD	Computer-aided Design
DV	Descent vehicle
FMI	Finnish Meteorological Institute
EDLS	Entry, Descent and Landing System
HEART	High Energy Atmospheric Reentry Test
LA	Lavochkin Association
CFD	Computational Fluid Dynamics
RITD	Re-entry: inflatable technology development in Russian collaboration
NASA	National Aeronautics and Space Administration
MIBD	Main Inflatable Braking Device
AIBD	Additional Inflatable Braking Device
MCD	Mars Climate Database

List of symbols

Symbol	description
a_1	constant in the turbulence model
A	(reference) area
c	speed of sound
$\bar{c}$	reference length
c_f	friction coefficient
c_p	heat capacity at constant pressure
C_A	axial force coefficient
C_D	drag coefficient
C_m	pitching moment coefficient
C_{m_α}	pitching moment coefficient slope with respect to the angle of attack
C_{m_q}	pitching moment coefficient slope with respect to the pitch rate
C_N	normal force coefficient
C_{N_α}	normal force coefficient slope with respect to the angle of attack
Cn	Courant number
C_L	lift coefficient
C_{L_α}	lift coefficient slope with respect to the angle of attack
D	diameter
E	total internal energy
F_i	flux in the ith cell
$\hat{F}$	flux through a cell face
F_1, F_2	blending functions
F_A	axial force
F_N	normal force
g	acceleration of gravity
g_m	$\approx 3.71\ \frac{\mathrm{m}}{\mathrm{s}}$, acceleration of gravity on the surface of Mars

h	enthalpy
h	altitude
$\vec{i}$, $\vec{j}$, $\vec{k}$	direction (unit) vectors
I_z	mass moment of inertia
k	kinetic energy of turbulence
Kn	Knudsen number
$\frac{L}{D}$	lift-to-drag ratio
L_s	solar longitude, the angle between Mars and the Sun
M	moment
Ma	Mach number
N	number of values
n_j	surface unit normal on a computational cell
p	pressure
P	production of kinetic energy
q	pitch rate
q_∞	$= \frac{1}{2}\rho U^2$, the dynamic pressure
Q	arbitrary quantity
Q_s, Q_i	source term
R	specific gas constant
Re	Reynolds number referred to the main diameter
Re_x	Reynolds number referred to the x-coordinate
R_m	≈ 3386 km, the average radius of Mars
$s_{i,j}$	mean strain-rate tensor
S	reference area
S	norm of strain-rate tensor
S_{cell}	face area
t	time
T	temperature
T_∞	free stream temperature
u_i	velocity component
U, $\vec{U}$	free stream velocity; vehicle velocity magnitude
U_τ	friction velocity
V_i	volume of a computation cell
W	vehicle weight
$x_i, x, y, z,$	coordinates
y^+	dimensionless distance from the wall
α	angle of attack
$\dot{\alpha}$	time derivative of the angle of attack
$\ddot{\alpha}$	second time derivative of the angle of attack
β_w	ballistic coefficient, calculated using the vehicle weight

β_m	traditional ballistic coefficient, calculated using the vehicle mass
β,β_1, β_2, β^*	constants in the turbulence model
Δ	difference
$\delta_{i,j}$	Kronecker delta. $\delta_{i,j} = 1$ if $i = j$, and 0 otherwise.
Δs	height of the first mesh cell
Δt	time step
ϵ	turbulent dissipation
γ	specific heat ratio
γ	trajectory angle in radians
γ_1, γ_2	coefficients in the turbulence model
$\lambda_{1,2}$	roots of the characteristic equation
μ	dynamic viscosity
μ_T	turbulent eddy viscosity
ω	specific rate of dissipation of the turbulence kinetic energy
ρ	medium density
σ_{k1}, σ_{k2}, $\sigma_{\omega1}$, $\sigma_{\omega2}$	constants in the turbulence model
τ_w	wall shear stress
$\overline{\overline{\tau}}$, $\tau_{i,j}$	viscous stress tensor

Contents

Chapter 1

Introduction and background

Within the framework of Mars exploration, the MetNet landing vehicle is a relatively new concept aimed to simplify and decrease the overall mass of the Entry, Descent and Landing Systems (EDLS). The current Mars rover concepts, for example, are using an aeroshell, a parachute, airbags and a dedicated lander structure or retro rockets [1, 2]. The MetNet concept, developed in collaboration by the Finnish Meteorological Institute (FMI), Instituto Nacional de Técnica Aeroespacial (INTA), and the Russian Space Research Institute, consists of deploying a pair of inflatable entry and descent systems, eliminating the need for a parachute or thrusters and a rigid heat shield [3]. This way, the ratio of payload mass to overall mass could be increased and hence the mission payload efficiency is improved. See Figure 1.1 for the landing scheme of the vehicle.

Shorthand for "Meteorological Network", the MetNet project (a larger idea than only the lander) aspires to set up a network of science stations around the surface of Mars. These stations, equipped with a multitude of instruments, would survey the Martian atmosphere, meteorology, planetary interior, crust, and also magnetic environment performing simultaneous observations at various locations on the Martian surface. This network would greatly enhance our view of the atmospheric conditions on Mars on a large scale, compared with the local results acquired by the previous landers and rovers. As the first step the mission plans to include deploying one precursor lander to Mars in 2022–2024 in order to demonstrate the technical robustness and scientific potential of the MetNet Mission concept.

The MetNet vehicle design started in the year 2001 and an EDLS body prototype was built between 2001 and 2004. Wind tunnel and heat flux tests have been conducted for the key components of the structure, but the problem with these tests is that it is difficult to replicate the actual descent and landing conditions on Mars. This is because the composition of the

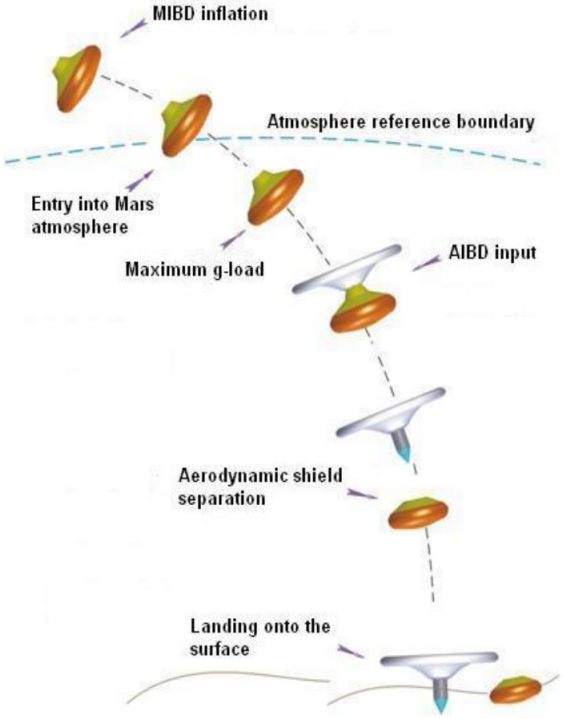

Figure 1.1: The descent phase of the MetNet lander [4].

atmosphere in Mars differs greatly from that on Earth. Even though the speed of sound in these conditions is of the same order of magnitude as on Earth, the Mach number will still be large (exceeding Ma = 20). Thus it is out of the question to make one-to-one tests of the mission. [3, 5]

Since no similar landers have been sent to Mars before, a lot of research has to be done in order to verify its feasibility and to predict whether the chosen concept will succeed in the mission. There have been simulations and tests of the structure, but a dedicated analysis and discussion about the aerodynamic stability of the descent vehicle is still missing. This thesis covers that topic. In 2014, FMI expressed the need for such work to the Fluid Mechanics Group of the Mechanical Engineering Department at the Aalto University and the project started in January 2015. In September 2015, the project was on display in European Planetary Science Congress 2015 [6].

Since analytical analyses of the complex geometry of the descent vehicle are close to impossible, numerical CFD-simulations are carried out. The analysis software of choice in this case is FINFLO. FINFLO is a general flow solver based on the numerical solution of the differential equations describing viscous flow (the so-called Navier-Stokes equations). Originally developed for

the solution of compressible flows, FINFLO should be fit for the task thanks to its efficiency, turbulence modeling capabilities and its ability to solve complicated three-dimensional flow cases. It has already been used successfully in many tasks in the fields of aerodynamics and applied thermodynamics [7].

The goal of the simulations is to acquire the aerodynamic features of the vehicle in the applicable configurations (the varying parameters will be the angle of attack, the Reynolds number and the Mach number) and heat flux data during the descent and landing phases. From the former it is possible to draw conclusions of the aerodynamic stability of the vehicle. Should it be aerodynamically unstable, the EDLS design would have to be considerably modified before sending the landing craft to Mars. Thus careful analysis of these features is in a decisive role in the development of the MetNet landing vehicle.

In this thesis, the aforementioned simulations are performed and conclusions are drawn from the analysis results. Trajectory calculations are also performed in order to support the CFD simulations and to predict the pertinent quantities related to the descent phase of the vehicle. Combined, these results form the aerodynamic analysis of the vehicle to the extent that is necessary in its design.

This thesis was made in the facilities of the Fluid Mechanics Group in Otaniemi during the year 2015. It serves as the final thesis for the degree of Master of Science.

Chapter 2

The MetNet Entry and Descent System

2.1 Background and history

The idea for the lander was first conceived in the 1980's by the FMI, the Russian Space Research Institute, Lavochkin Association (LA) and Instituto Nacional de Técnica Aeroespacial. However, it was only in 2000 that the development work started. During the evolution of the project, five different descent system scenarios were analysed and a prototype was manufactured in 2002. Martian environmental qualification testing was performed for the entry, descent and landing components of the selected variant. [3, 8, 9].

MetNet has generated several spin-off projects, including the NASA projects called the High Energy Atmospheric Reentry Test and the Hypersonic Inflatable Aerodynamic Decelerator, and MetNet Entry, Descent and Landing System (EDLS) for Earth Reentry (RITD), as well as a MetNet precursor mission (MMPM). The RITD concept, for example, consists of the same lander structure as in the MetNet Mars lander project (the main focus of this work) but with the intention of using it on Earth re-entry. This would benefit the existing projects already on Earth's orbit by facilitating the logistics between an orbiter and our planet. The MMPM project aims to send one or two MetNet descent vehicles to Mars, serving as a technology and science demonstration mission.

The most recent advancements of the MetNet project have been the improvement of Mars' atmospheric model [10], a mathematical modelling of the lander [11], the aforementioned wind tunnel tests [12, 13], feasibility analyses [14] and analysis of dynamic stability of the lander in the transonic flow regime [15]. The latter is clearly useful also in this thesis, even though the

analyses were done with an atmospheric model of the Earth and with a relatively low Mach number (the maximum Mach number in that document was Ma $\approx$ 2). The observations in the documents suggest that, in order to increase its dynamic stability, the vehicle be given angular speed around its axis of symmetry during the entry phase:

> (...) to provide MetNet DV stability in upper atmospheric layers the angular rate of spinning after Main Inflatable Braking Device (MIBD) inflation should make 60 deg/s [15].

Additionally, it was concluded that the simulations resulted in static stability on certain conditions:

> MetNet DV with inflated MIBD is statically stable at Knudsen numbers < 0.3 and at continuous flow within the whole range of Mach numbers [15].

It was also noted that in the subsonic regime the vehicle would portray dynamic instabilities in some cases, resulting in more constraints and requirements for the entry and landing phases.

2.2 Mars atmospheric entry and descent conditions

Analysing and understanding the atmospheric conditions on Mars is essential in this project, since they directly influence the aerodynamic characteristics of the lander. The speed of sound, for example, dictates the behaviour of shock waves in the flow. In this section, the pertinent quantities are obtained by deducing values from existing data and documentation.

In order to acquire the parameters related to the atmospheric conditions where the vehicle is designed to operate, alongside with other documentation, an on-line service called The Mars Climate Database is used [16]. Their documentation gives a good representation of the service:

> The Mars Climate Database (MCD) is a database of atmospheric statistics compiled from state-of-the art Global Climate Model (GCM) simulations of the Martian atmosphere.
>
> The GCM computes in 3D the atmospheric circulation taking into account radiative transfer through the gaseous atmospheres as well as through dust and ice aerosols, includes a representation of the CO_2 ice condensation and sublimation on the ground and in the atmosphere.

> The model used to compile the statistics has been extensively validated using available observational data and aims at representing the current best knowledge of the state of the Martian atmosphere given the observations and the physical laws which govern the atmospheric circulation and surface conditions on the planet [17].

The service thus gives plausible initial values for our simulations. The relevant parameters are the medium density and viscosity, atmospheric temperature and the speed of sound in the medium. MCD can provide the first three of these; the speed of sound has to be derived from the available information and a relation between the mentioned quantities.

2.2.1 Dependence of time and space

Before any calculations are made, it is important to take into consideration how these quantities vary with space and time. Let us examine temperature, since it affects the value of many quantities. This can be carried out by comparing temperature maps (see Figure 2.1) of the Martian surface.

As can be seen from Figure 2.1, the temperature is the lowest, as one can expect, in the polar areas. Closer to the equator (latitude ≈ 0) the temperature is always higher by tens of Kelvins. Along the longitude, there is also a warmer region (the positive longitudes in the figure). This area corresponds to the areas that are facing the Sun at a given time. In other words, it is daytime in those areas. Thus the longitudinal differences correspond to day-vs-night differences.

Seasonal changes also have an effect on the temperature distribution. The warm region (the dark area in the figure) moves in latitude when the solar longitude L_s changes. At summer solstice ($L_s = 90°$) the warm region is in the north and at winter solstice ($L_s = 270°$) in the south. The movement of the warm region can be seen by setting the altitude to zero.

It can be seen (and shown by statistics) that the night-vs-day changes are significant. As a rule of thumb it can be said that the temperature on the surface during the night is 50 K lower than during the day. The difference between “summer” and “winter” is approximately the same. It must be kept in mind that these results apply to the surface only.

2.2.2 Gas state equation

A crucial model that will be directly fed into FINFLO is an equation of state for the gas. Therefore, it is essential to examine results from MCD and see

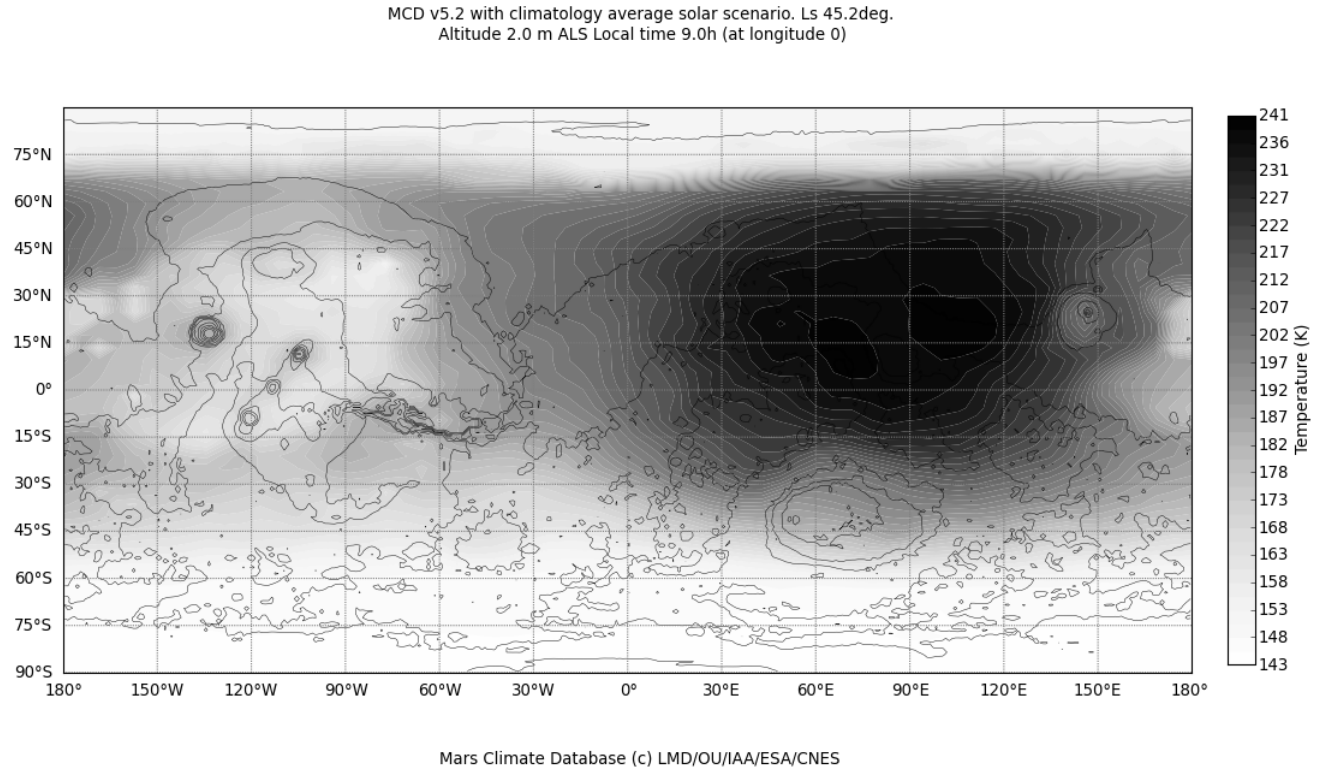

Figure 2.1: An example of mapping the temperature on Mars [16].

if the ideal gas assumption can be made. This would imply that the relation $p = \rho RT$ holds. If this is assumed, the behaviour of R, the specific gas constant, can be studied by extracting graphs of pressure, density and temperature across the red planet. Now, the set of points $(\rho T, p)_i$, $i = 1, 2, ..., n$ should represent approximately a line with a least-squares slope

$$R = \frac{\sum_{i=1}^{n} \rho_i T_i p_i}{\sum_{i=1}^{n} \rho_i^2 T_i^2}, \tag{2.1}$$

where ρ is the medium density, T is the medium temperature and p is pressure. It turns out that the ideal gas approximation is correct with negligible deviation and, therefore, the ideal gas assumption will be applied henceforth. One of the datasets is partially retained in Table 2.1. The slope R is approximately independent of time and space. By comparing different values from different altitudes, times and locations, the value obtained is $R \approx 190 \pm 0.4 \ \frac{\text{J}}{\text{kgK}}$ $(N = 40)$. These results were obtained from several sets of data, gathered in several locations on Mars.

Table 2.1: Example data for calculating R. The solar longitude was set to $L_s = 225.0°$. Longitude 30.0E, Altitude 1000.0 m, ALS Local time 12.0 h (at all longitudes).

ρ $\left[\frac{\text{kg}}{\text{m}^3}\right]$	T [K]	p [Pa]	ρT	ρRT
0.0106	186.4330	370.7860	1.9786	376.0993
0.0108	183.0520	370.0510	1.9761	375.6183
0.0136	173.6950	444.2280	2.3637	449.2938
⋮	⋮	⋮	⋮	⋮
0.0221	148.8300	627.9430	3.2927	625.8869
0.0213	147.9230	600.5140	3.1479	598.3693
0.0193	147.2660	543.4940	2.8488	541.5202

2.2.3 The speed of sound on Mars

In *Project Documentation for Selected concept* by LA [5], some values can be found for the velocity and Mach number of the case. The speed of sound can thus be calculated from that data. Table 2.2 shows the data from the document and the results for the speed of sound. The deduced speed of sound was obtained by dividing the velocity by the reported Mach number. The MARS-GRAM 2001 atmospheric model was used to obtain these values. Validation of the model has indicated a "generally good" agreement with MCD for density [18] but no comments were made on the speed of sound. Some calculations by hand should therefore be made to verify these results.

According to Miettinen [19], the speed of sound can be calculated from

$$\frac{1}{c^2} = \frac{1}{\rho}\frac{\partial \rho}{\partial h}\bigg|_p + \frac{\partial \rho}{\partial p}\bigg|_h, \tag{2.2}$$

where c is the speed of sound and h is enthalpy. His work also gives the relations

$$\frac{\partial \rho}{\partial h}\bigg|_p = \frac{1}{c_p}\frac{\partial \rho}{\partial T}\bigg|_p \tag{2.3}$$

$$\frac{\partial \rho}{\partial p}\bigg|_h = \frac{\partial \rho}{\partial p}\bigg|_T - \frac{1}{\rho c_p}\frac{\partial \rho}{\partial T}\bigg|_p \left(1 + \frac{T}{\rho}\frac{\partial \rho}{\partial T}\bigg|_p\right) \tag{2.4}$$

Combining these gives

$$\frac{1}{c^2} = \frac{1}{\rho c_p}\frac{\partial \rho}{\partial T}\bigg|_p + \frac{\partial \rho}{\partial p}\bigg|_T - \frac{1}{\rho c_p}\frac{\partial \rho}{\partial T}\bigg|_p \left(1 + \frac{T}{\rho}\frac{\partial \rho}{\partial T}\bigg|_p\right) = \frac{\partial \rho}{\partial p}\bigg|_T - \frac{T}{\rho^2 c_p}\left(\frac{\partial \rho}{\partial T}\bigg|_p\right)^2 \tag{2.5}$$

As was noted before, the ideal gas assumption can be used. This implies

$$\rho = \frac{p}{RT} \qquad \Rightarrow \begin{cases} \frac{\partial \rho}{\partial p}\Big|_T = \frac{1}{RT} \\ \frac{\partial \rho}{\partial T}\Big|_p = -\frac{p}{RT^2} \end{cases} \tag{2.6}$$

Now the equation for the speed of sound becomes simply

$$c = \sqrt{\frac{c_p}{c_p - R} RT} \tag{2.7}$$

This is merely a different formulation of $c = \sqrt{\gamma RT}$, where γ is the specific heat ratio, but more useful since the value of γ is not directly available.

The values of c_p can be directly obtained from MCD and the scalar maps reveal that it is strongly dependent of temperature. Since R is a constant, we can conclude that c is significantly dependent of T only.

For the purposes of this work, it would be very useful to tabulate values for c. For this, we can use the conclusions made about the temperature distribution, ie. that it can be separated into "hot" and "cold" regions that correspond to night-vs-day changes and seasonal changes.

The values for T and c_p were obtained so that $L_s = 0$, local time 8 hours (at longitude 0). This way the hot values correspond approximately to positive longitudes and the cold ones to negative longitudes. Two graphs were obtained for each altitude: latitude ± 10 degrees. The positive and negative longitudes were separated and the two different latitudes were treated together in order to increase the number of obtained values. Now the values for c were calculated from Equation (2.7). The value of γ was also computed and averaged. The standard deviations for c were also computed.

The results are presented in Table 2.3. Since there was some deviation in the values for c, the 95 % confidence intervals have been calculated ($N = 64$). These have been drawn to Figure 2.2. As can be seen, the values from LA agree quite well with cold conditions and thus these values can be used from now on. Although the deviations in the value are significant, a rule-of-thumb will be useful for later purposes. With regression, the following equation can be made:

Table 2.2: Values from "MML movement parameters (variant A)" [5].

Descent stage	Altitude [km]	Velocity $\left[\frac{\text{m}}{\text{s}}\right]$	Mach number	Deduced speed of sound $\left[\frac{\text{m}}{\text{s}}\right]$
Atmospheric entry	120	6080	28.39	214.2
Maximal g-load	30	3958	19.55	202.5
PC cover jettisoning, PS deployment	8.41	296	1.309	226.1
MP unriffing	7.72	84.72	0.373	227.1
AS separating, start of SM suspension (...)	7.58	50.95	0.224	227.5
Finish of ISD inflating and SM hanging	7.36	20.16	0.089	226.5
Landing on the level $H = 2$ km	2.00	23.68	0.102	232.2
Landing on the level $H = 0$ km	0.00	21.70	0.093	233.3

Table 2.3: The speed of sound and heat capacity ratio γ on Mars as a function of altitude. The values have been obtained from Mars Climate Database.

	Cold			Hot		
Altitude [km]	Average $\left[\frac{\text{m}}{\text{s}}\right]$	std. deviation $\left[\frac{\text{m}}{\text{s}}\right]$	γ	Average $\left[\frac{\text{m}}{\text{s}}\right]$	std. deviation $\left[\frac{\text{m}}{\text{s}}\right]$	γ
0.0	215.203	7.643	1.360	249.723	14.761	1.310
0.5	231.867	4.092	1.332	241.041	4.735	1.319
1.0	233.313	3.910	1.330	240.337	4.230	1.320
4.0	232.368	3.599	1.332	235.786	2.265	1.327
8.0	228.970	4.350	1.337	232.338	1.707	1.332
12	225.003	5.154	1.343	228.325	2.006	1.338
20	218.346	3.802	1.354	220.903	1.684	1.349
30	212.869	2.359	1.363	211.384	1.404	1.366
40	208.287	2.499	1.372	205.845	1.564	1.376
50	201.194	4.412	1.386	199.642	2.752	1.389
75	191.149	4.599	1.408	197.896	6.862	1.393
100	181.952	3.489	1.424	183.618	6.943	1.425
120	186.894	4.452	1.390	186.176	9.587	1.404

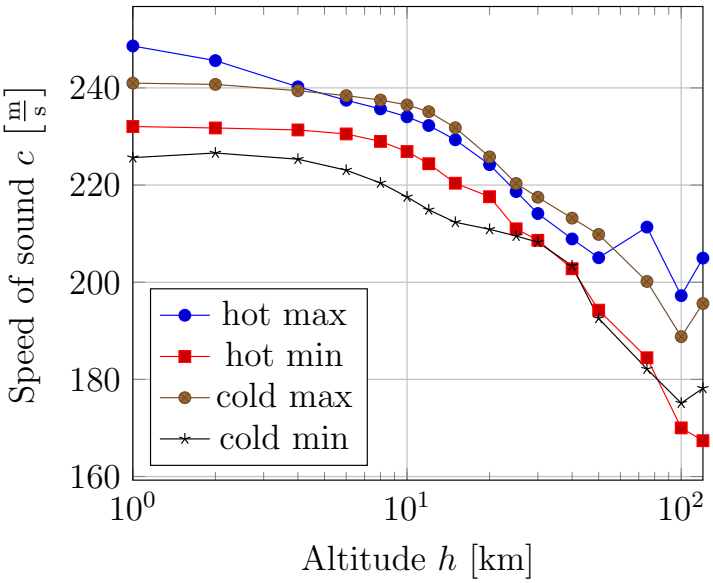

Figure 2.2: The speed of sound as a function of altitude. The "min" and "max" values correspond to 95 % confidence interval limits, and hot and cold correspond to day-vs-night or seasonal changes.

$$c(h) \approx 236.8e^{-0.00247h}, \tag{2.8}$$

where the altitude h is given in kilometres. The calculated values of γ have also been plotted in Figure 2.3. We can see that its value rises with altitude and seasonal changes have only a very small effect.

From the same data that was used to generate the previous results, we can also make a rule-of-thumb for the average temperature as a function of altitude. The temperature data is plotted into Figure 2.4. The resulted regression obtained from averaging cold and hot conditions is

$$T(h) \approx 226 - 4.5 \ln^2 (1 + h), \tag{2.9}$$

where the +1-term was added to avoid numeric problems near the surface. Here h is again the altitude in kilometres. The coefficient of determination for this approximation is roughly 0.988. As can be seen from Figure 2.4, the temperatures have relatively large variations even when they are quantized for the hot and cold areas. If the exact location of the lander is unknown, it is difficult to estimate the temperature with accuracy lower than 10 K. The error is quite large in every case and a rough approximation like that of Equation (2.9) can be made.

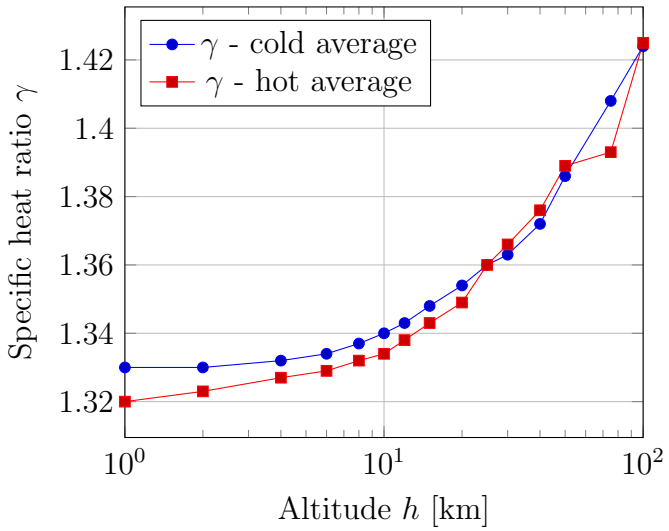

Figure 2.3: The heat capacity ratio γ as a function of altitude. The hot and cold correspond to day-vs-night or seasonal changes.

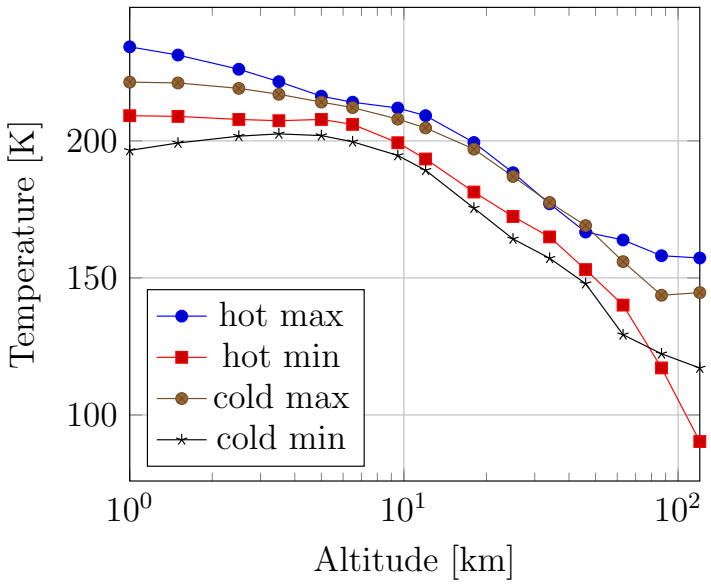

Figure 2.4: The average temperature as a function of altitude, from dataset obtained for Figure 2.2. The "min" and "max" values correspond to 95 % confidence interval limits, and hot and cold correspond to day-vs-night or seasonal changes.

Table 2.4: Gas density as a function of altitude, gathered from MCD [16].

Altitude [km]	Density $\rho \times 10^3$ $\left[\frac{\text{kg}}{\text{m}^3}\right]$
0.1	16.3123
0.5	15.5141
1.0	14.6476
2.0	13.2072
5.0	10.0122
11	5.8476
25	1.75124
37	0.42658
55	0.05515
80	0.002187
100	0.000167
120	0.0000109
140	0.0000006

2.2.4 Atmospheric density

Even though the seasonal fluctuation of density is significant at certain time periods, quantifying these differences would not contribute to this work. This is because the seasonal changes are of the order of 10 %. The aerodynamics of the vehicle are not very sensitive to the Reynolds number, so this kind of error does not impair the results of this work. Thus we only make an approximation of the density as a function of altitude and around the latitude zero at a given season.

The results were collected by obtaining two sets of values from each altitude: latitudes $\pm 30°$ and the global average was calculated for these. Time setting was chosen to be $L_s = 0°$, local time 9 hours. The results are in Table 2.4. A regression for the logarithm of density gives:

$$\rho(h) \approx \begin{cases} e^{-4.113-0.095h} & \text{if } h \leq 46 \text{ km} \\ e^{-2.320-0.134h} & \text{if } h > 46 \text{ km} \end{cases}, \tag{2.10}$$

where h is in kilometres. This gives a coefficient of determination of 0.998 and thus it can be used as a rule-of-thumb for the density in this work. The equation was cut into two pieces in order to increase accuracy at high altitudes. Additionally, in Figure 2.5 is a graph of the results for the medium density. The results from LA documentation were also drawn into the graph and they are in good agreement as expected.

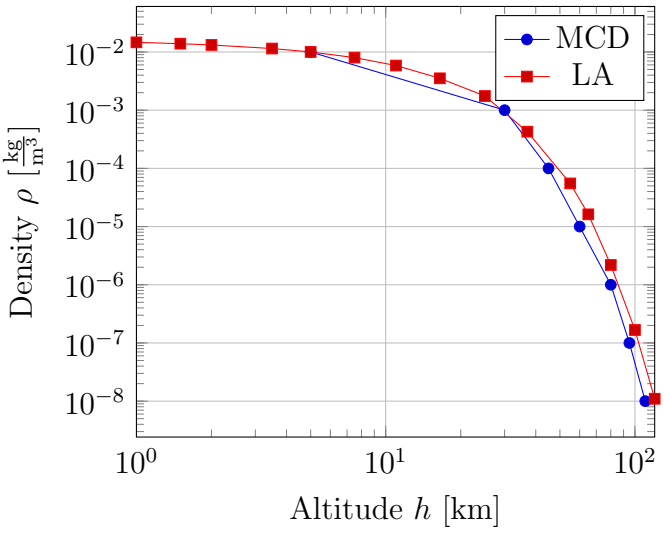

Figure 2.5: Medium density as a function of altitude. Results are plotted directly from MCD and from LA documentation [5].

2.2.5 Atmospheric viscosity and Sutherland coefficients

The dynamic viscosity of the medium can be calculated from the Sutherland Law. It was observed that this relation is independent of time and location, and data gathered from MCD can be used to give the following relation:

$$\mu \approx 1.92 \times 10^{-7} \frac{T^{1.8}}{T + 60} \tag{2.11}$$

The coefficients were determined by the least-squares method. This approximation gives a coefficient of determination larger than 0.999 in all cases and thus we have all the reason to believe that this is very close to the form used in MCD. Now the viscosity as a function of altitude is obtained by inserting Equation (2.9) into this result.

2.3 The vehicle & landing phases

The MetNet DV is a set of subsystems, each designed for their own purpose and a specific phase of the flight. Different phases have largely different geometries. In other words, the apparatus changes its form during the entry and landing phases. Gases are used to inflate the new parts in the geometry: It uses two inflatable breaking units. The following subsections discuss these phases and geometries in detail. It should be noted that in this work it is not important to consider the interior of the lander (because it has little effect on

the aerodynamic characteristics of the vehicle; and because the interior parts are not modeled in the simulations) and thus only the outside geometry is considered.

2.3.1 MetNet DV in the transport configuration

Figure 2.6 depicts the MetNet DV in the transport configuration, ie. in the configuration it has right when it is launched or dropped from the vehicle that was carrying it. This configuration occupies the least amount of space (the main dimensions are roughly 500×600 mm^2), enabling several vehicles on board a modern spacecraft. At this point, the mass of the vehicle is roughly 22.2 kg. [20]

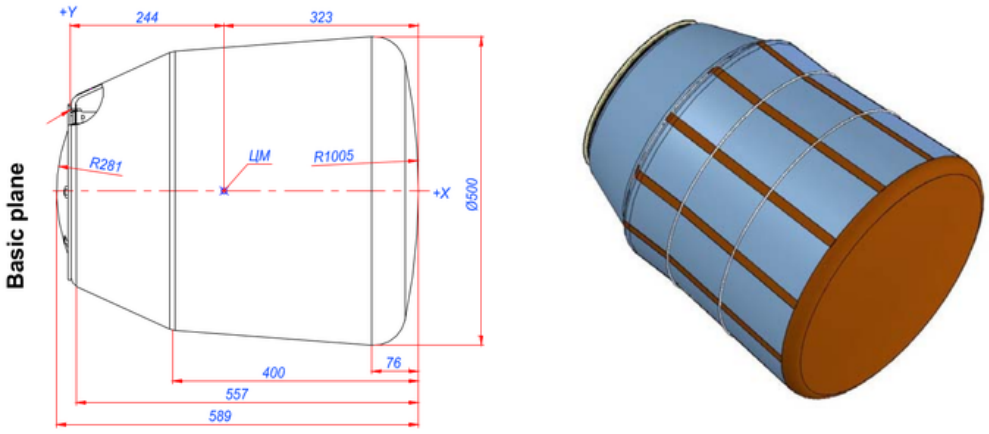

Figure 2.6: MetNet DV in transport configuration with main dimensions [15]. The symbols "Цм" in the schematic picture are short for "Центр масс", the centre of mass.

This phase is not treated in this thesis because it is not part of the entry phase. However, in order to ensure the intended landing procedure, this configuration must stay approximately aligned with its velocity vector (to the right in the figure). Since this configuration is designed to approach Mars at a very high altitude and essentially in a vacuum, the assumption will be made that any aerodynamic effects will be negligible at this point. Therefore, we can assume that the vehicle remains aligned in this phase.

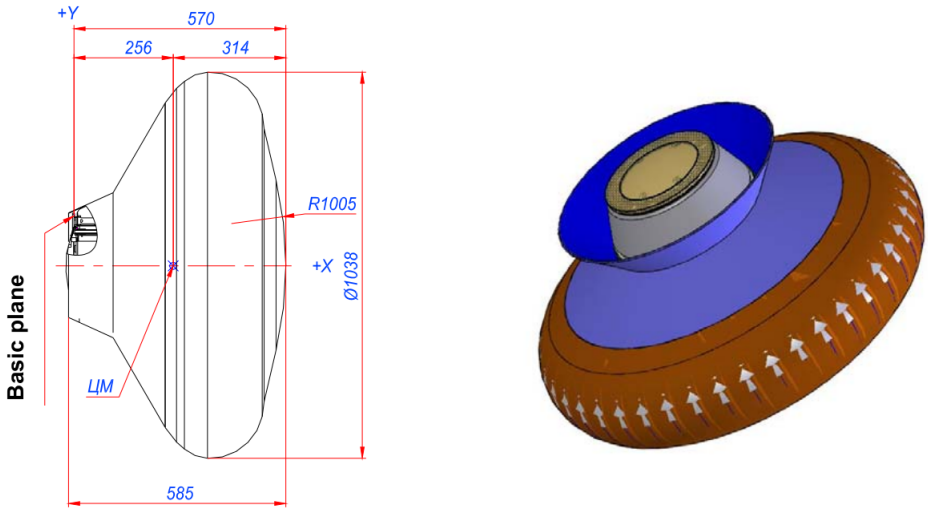

Figure 2.7: MetNet DV with inflated MIBD [15].

2.3.2 MetNet DV with inflated Main Inflatable Braking Device (MIBD)

When approaching and entering to the Martian atmosphere, the vehicle will inflate the main inflatable braking device. The new geometry is depicted in Figure 2.7. In this configuration, the vehicle (with a mass of still roughly 22 kg [20]) will travel across a major part of the total distance to the ground; the entry phase into the atmosphere will begin from a nominal value of 120 km [15] and the next phase will not be inflated before an altitude of about 8 to 12 kilometres. The design entry velocity is 4586 $\frac{\text{m}}{\text{s}}$ with a Mach number of Ma $\approx$ 26 [4].

One parameter of considerable interest in LA's previous work has been the Knudsen number, defined as the ratio of the molecular mean free path length and a reference length. A small Knudsen number (generally Kn < 0.2) implies that the continuum approximation can be made. This poses a limit for the simulations, because this approximation is made in FINFLO. At larger Knudsen numbers, equivalent to free molecular regime, the results would become flawed. The Knudsen number can be tied to the Reynolds number, defined as

$$\text{Re} = \frac{\rho U D}{\mu}, \tag{2.12}$$

where U is the free stream velocity and D is the reference length, ie. the

diameter of the vehicle. It can be shown that [21]

$$\mathrm{Kn} = \frac{\mathrm{Ma}}{\mathrm{Re}}\sqrt{\frac{\gamma\pi}{2}} \tag{2.13}$$

Equation (2.13) can be used to make an approximation for the altitude limiting the region of the continuum approximation. Inserting the definitions of the Mach number and the Reynolds number, the equation becomes

$$\mathrm{Kn}(h) = \frac{\mu(h)}{\rho(h)c(h)D}\sqrt{\frac{\gamma\pi}{2}} < 0.2 \tag{2.14}$$

Now equations (2.8)-(2.11) can be used to solve the maximum altitude for the continuum approximation numerically. As the diameter of the vehicle in the higher altitudes is $D = 1$ m, the result is approximately $h < 97.5$ km.

2.3.3 MetNet DV after the inflation of Additional Inflatable Braking Device (AIBD)

In order to further decelerate the vehicle, an auxiliary inflatable braking device (AIBD) is deployed. The new configuration is shown in Figure 2.8. As can be seen from the image, the newly inflated part is much larger than the first inflated part; its diameter is roughly twice that of MIBD. The mass of the vehicle is designed to be 13.81 kg at this point [20].

AIBD is deployed as soon as the Mach number descends to Ma = 0.8. The altitude at which this happens is not fixed since it depends on the entry angle. The airspeed will have descended below 200 $\frac{\mathrm{m}}{\mathrm{s}}$ at this point, and the Reynolds number will be in the range of Re = 100 000...200 000.

In this work it is assumed that MIBD will be jettisoned at the same time as AIBD is inflated; a case where they are both present will not be simulated. Thus the configuration after the jettison is what interests us and it is also the configuration whereby the MetNet lander will penetrate the surface of Mars. The design landing speed of the vehicle is 44...58 $\frac{\mathrm{m}}{\mathrm{s}}$.

2.4 Potential problems

The potential complications related to the landing phase of the MetNet lander can be divided into two categories: aerodynamic and thermodynamic problems.

In the transport configuration phase, there are little aerodynamic effects due to the negligible medium density. Thus any further aerodynamic analysis

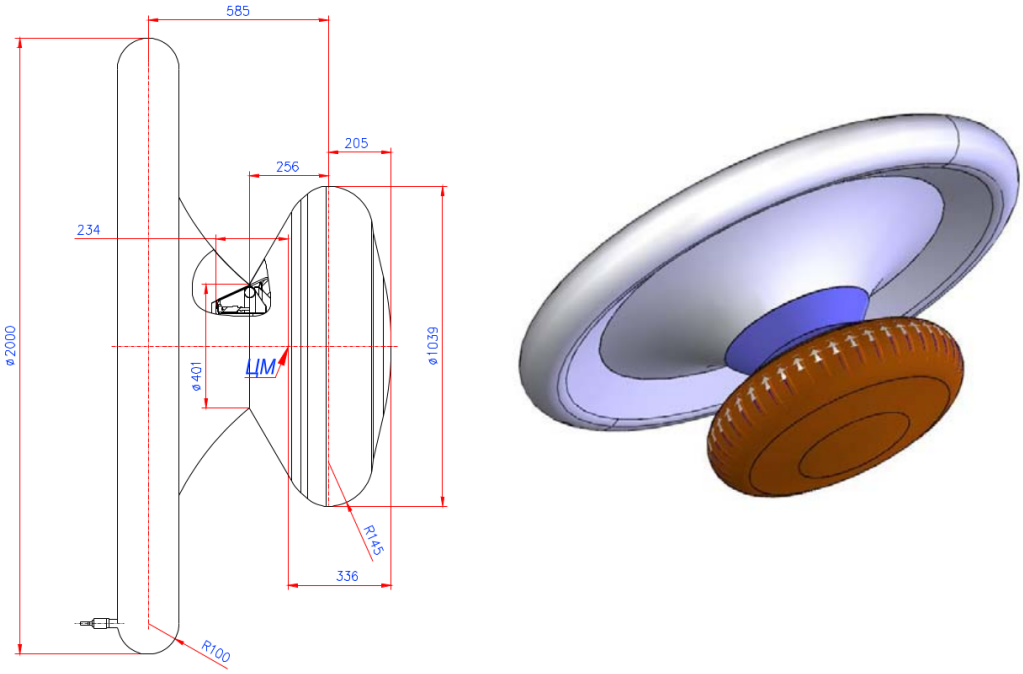

Figure 2.8: MetNet DV after AIBD inflation [15].

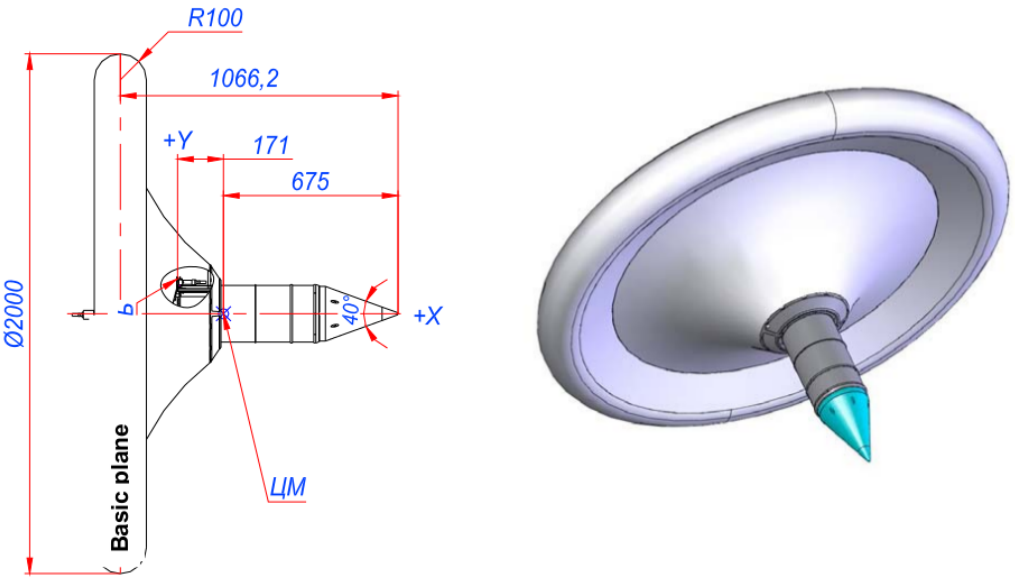

Figure 2.9: MetNet DV with inflated AIBD after jettison of MIBD [15].

of this phase can be ignored. However, the aerodynamics of the subsequent phases could impose requirements for the actual launch from the carrying vehicle. For example, as it has been noted, the vehicle should be given the angular speed, mentioned in Section 2.1, around its axis of symmetry. Also, the entry speed and angle are to be carefully chosen. Thermodynamic problems related to the transport configuration phase can also be dismissed due to the negligible medium density.

After the vehicle has entered the atmosphere, the aerodynamic effects can cause issues for the descent stage. It is imperative that the vehicle land upright. In other words, it must not turn over during the flight. This is called aerodynamic stability and it is the most important point in this work; the simulations and analyses aim to verify this condition. This requirement is equally important for the two phases discussed earlier. It is possible to estimate whether or not such a reversal will happen by creating a model of the movement of the vehicle around itself. Once such a model has been created, a condition for its stability can be formulated. This is carried out starting from Section 3.1. Also, the final speed, pertaining to the drag coefficient of the vehicle, needs to be under a certain limit value in order for the vehicle to be able to function properly after landing.

Another problem with AIBD is its size. It will take more time to inflate, compared to MIBD, and this could potentially be a problem for the aerodynamic effects and stability. If, for example, the part remains in a partially inflated state for a non-negligible time and, for this reason, the vehicle becomes asymmetric for some time, it is clear that the aerodynamic effects will also be asymmetric. This could cause the vehicle to become dynamically unstable. This problem is not covered in this work.

The imaginable thermodynamic problem of the landing phase is the excessive warming of the vehicle. LA has already produced some results for the heat fluxes during the descent phase, but the simulations in this work provide also some pertinent results.

2.5 Previous work

Documents from LA, FMI and Babakin Space Center provide documentation of analyses and tests done for the lander. In this section, the results are gathered and analysed in order to support and to provide reference values for this work. This way, the results of the simulations done in the context of this work can be easily compared with the values obtained by LA. The pertinent results are the wind tunnel tests (from which the important aerodynamic coefficients can be obtained), heat tests and drop tests.

A large part of the documentation is from the first years of the current century and the design has been altered a number of times. The numerical values of many parameters change between documents, the most noticeable ones being the diameters and the masses of the different configurations. In the latest documentation, *RITD Final Report* from 2015, the diameter is fixed to exactly $D = 1$ m for the MIBD phase and $D = 2$ m for the AIBD phase. The mass (in the transport phase) is fixed to 22.2 kg. In this document, the entry velocity is fixed to 4586 $\frac{\text{m}}{\text{s}}$ instead of the older value of 6080 $\frac{\text{m}}{\text{s}}$. [4]

2.5.1 Wind tunnel tests and their results

The first documented wind tunnel tests for the vehicle were performed by LA in the Institute of Mechanics of Moscow State University in 2002. Wind tunnel models of the two main configurations, MIBD and AIBD, were made, both of main diameter 80 mm. The two models are portrayed in Figure 2.10.

Figure 2.10: Models used in the wind tunnel tests conducted by LA in 2002 [22].

The models were placed in the wind tunnel with special holders in order to measure the static aerodynamic forces and to change the angle of attack (see Section 3.1) of the models. The range of Mach numbers tested was $0.43 \ldots 0.8$ (for AIBD) and $0.8 \ldots 2.54$ (for MIBD). The Reynolds number varied in the range of $\text{Re} = (0.7 \ldots 3.3) \times 10^6$, but in the results the actual value used was not given. The documentation also warns that there is approximately a 5% average error in the lift coefficient and an $8 \ldots 15\%$ error in the pitching moment coefficient. A flow field visualisation was also done using the Schlieren method, demonstrating the formation of shock waves. The numerical values are presented in the appendices in comparison with the simulation results.

More recent work conducted by LA in 2014 includes the wind tunnel tests of the MIBD configuration in order to determine its dynamic (transient) aerodynamic features. The studied coefficient is the pitch-damping coefficient, denoted in the work by $m_z^{\overline{\omega}_z}$ and more commonly by C_{m_q}. A model with a diameter of 74.2 mm was built using 3D printing technology. The model was placed in another wind tunnel but this time it was set up so that it can move freely after being given an initial angle of attack. This way it is possible to study the dynamic behaviour of the vehicle as a function of Mach number and the initial angle of attack. A high-speed camera was used to pick up the movements of the model.

In these tests, the free stream Mach number was $0.85 \ldots 1.53$ and the Reynolds number was $(1.25 \ldots 3.0) \times 10^5$, respectively [13]. When the flow in the tunnel was turned on, the model started to oscillate at a frequency between 10 and 20 Hz. The high speed camera tracked these movements. An interesting feature is the static angle of attack or the maximum (absolute) value of the angle of attack that the model reaches during each vibration cycle. For example, at $\mathrm{Ma} = 0.85$ and at an initial angle of attack of $10°$, the model started to oscillate, after approximately 0.2 seconds, between roughly $-10°$ and $10°$. Here the static angle of attack would be $10°$.

Following the evolution of the static angle of attack, the results can be summarised as follows:

- At $\mathrm{Ma} < 1$ pitch damping will occur at static angles of attack of $\alpha < 10°$. The static angle of attack will tend to zero.

- At $\mathrm{Ma} > 1$ the static angle of attack will gravitate to approximately $10°$ and oscillate around that value.

Cases with an initial angle of attack larger than $10°$ were not examined in these tests. The conclusion is that the dynamic wind tunnel tests do support the dynamic stability of the vehicle. In other words, the angle of attack stays restrained and the vehicle is dynamically stable (Lyapunov stable).

Other documentation can also be found where values for the aerodynamic coefficients are presented (for example in *Feasibility of MetNet EDLS to Earth re-entry* [20] and *Analysis of and inflatable EDLS' dynamic stability in the transonic regime* [15]), but the procedure by which these were obtained is not well explained: the only comment made is that they are "calculation results". Therefore, these values will be treated as estimations. However, the interesting feature of these results is that they also treat the case of flight in rarified gas. For this reason it is reasonable to also comment on these results.

In order to use these static results in the context of this work, further treatment must be given to the numerical values. This is because the coefficients given are the axial coefficient C_A and the normal coefficient C_N whereas the coefficients we are interested in are the lift coefficient C_L and drag coefficient C_D (see Section 3.1). The conversion between these is

$$\begin{aligned} C_L &= C_N \cos\alpha - C_A \sin\alpha \\ C_D &= C_N \sin\alpha + C_A \cos\alpha \end{aligned} \tag{2.15}$$

It is crucial to note that in LA's convention, the angle of attack is defined as exactly the opposite to our definition. Therefore, when converting these results, a negative value must be used for α. An example result from the transformation is in Figure 2.11.

Additionally, the pitching moment coefficient is calculated with respect to different points. LA's calculation results were tabulated with respect to the nose of the vehicle [15], whereas the FINFLO results are calculated with respect to the centre of mass. The conversion between these can be calculated from

$$C_{m_{\text{com}}} = C_{m_{\text{nose}}} + C_N \frac{x_{\text{com}} - x_{\text{nose}}}{D}, \tag{2.16}$$

where $C_{m_{\text{com}}}$ and $C_{m_{\text{nose}}}$ are the pitching moment coefficients relative to the centre of mass and nose, respectively, and x_{com} and x_{nose} are the locations of the centre of mass and the nose, respectively, in the chosen coordinate system. For the case of MIBD (see Figure 2.7), we see that $x_{\text{com}} - x_{\text{nose}} \approx 314$ mm. As for AIBD (see Figure 2.9), the corresponding value is $x_{\text{com}} - x_{\text{nose}} \approx 675$ mm.

After the treatment for the values for MIBD [15], the following general trends can be seen:

- In the large Knudsen number regime (rarified gas) the drag coefficient C_D is approximately between 1.5 and 2 for realistic angles of attack ($\alpha < 30°$) and diminishes with growing α. For lower Knudsen numbers (continuous flow) the value is approximately 1.0 for small Mach numbers and raises to 1.4 for the larger Mach numbers.

- The absolute value of the lift coefficient C_L grows in a linear fashion for realistic angles of attack, as expected. The slope $C_{L_\alpha} = \frac{\partial C_L}{\partial \alpha}$ is approximately $-0.8\ \frac{1}{\text{rad}}$ for small Knudsen numbers and $-0.1\ \frac{1}{\text{rad}}$ for large Knudsen numbers.

- The pitching moment coefficient about the centre of mass is positive for large Knudsen numbers and negative for small Knudsen numbers.

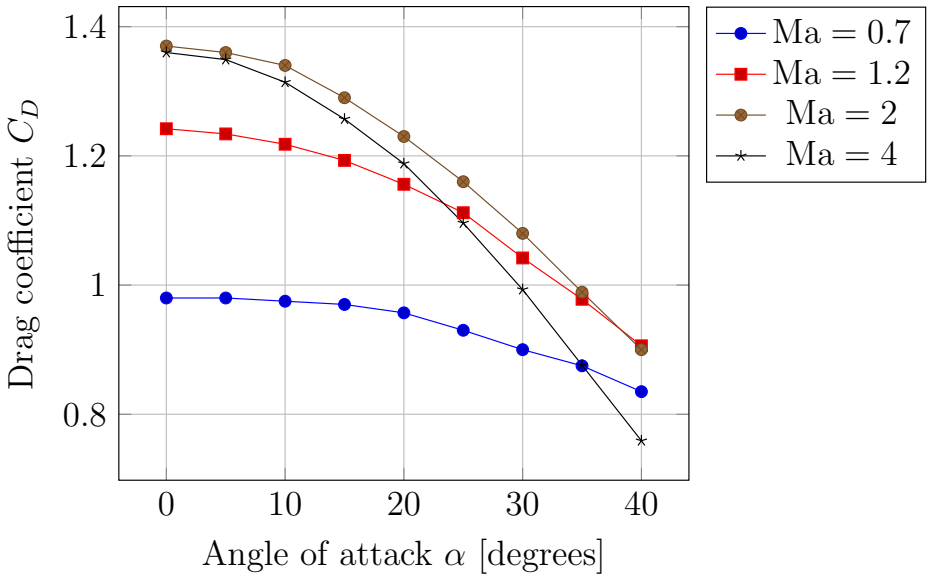

Figure 2.11: Drag coefficient values for MIBD after the coordinate transformation (Equation (2.15)) for the case of a small Knudsen number. Original values are extracted from documentation by LA [15].

The same coefficient about the vehicle "tip" or the fore is negative for any Knudsen number.

The results for the deployed AIBD (in this case the Knudsen number is always small, since it is deployed when the vehicle is relatively close to the Martian surface) from the same document indicate the following:

- The drag coefficient C_D is approximately 1.
- The normal force coefficient slope C_{N_α} is of the order of 0.1
- The pitching moment coefficient slope C_{m_α} is of the order of -0.6, but might turn positive for small Mach numbers (Ma ≈ 0.1)
- The pitch rate slope C_{m_q} (see Section 3.3), in transonic flow is positive for small angles of attack but negative at smaller Mach numbers.

The smallest Mach number that the AIBD configuration will encounter is of the order

$$\text{Ma} = \frac{\text{Surface landing speed}}{\text{Speed of sound at altitude 0 m}} \approx \frac{50\ \frac{\text{m}}{\text{s}}}{236.8\ \frac{\text{m}}{\text{s}}} \approx 0.2 > 0.1$$

Therefore, it is likely that, according to the previous results, the pitching moment coefficient slope stays negative. This indicates static stability for the AIBD configuration. In the dynamic regime, the fourth conclusion in the previous results suggests that right after the AIBD deployment the static angle of attack would not be 0 degrees but about five to ten degrees. Thus the only phase of the flight where the lander would not be (Lyapunov) stable, according to these results, is in the high Knudsen number regimes or at very high altitudes.

2.5.2 Heat transfer tests

Another concern of the MetNet project is the potential problems related to the thermodynamic effects or, in practise, the heating of the vehicle. This causes sublimation of the thermal protection coating applied to the vehicle and it could also damage the instruments in the payload. These effects have also been analysed by LA.

A calculation of the warming and ablation was documented in *Project Documentation for Selected Concept* in 2002. Fourier's law and heat equation was used in accordance with the Stefan–Boltzmann law for the boundary conditions. With these, the heat fluxes and temperatures were calculated as a function of time at several points around the vehicle. When the properties of the thermal protection coating were known, the amount of linear ablation (material loss in millimeters) was also calculated. The atmospheric entry angle was selected to be 12° [5].

The results from this document indicate that the maximum temperature reached during the descent stage is just under 700 °C right on the surface of the vehicle. The temperature of the internal structure would not surpass 200 °C. Ablation of the protective coating was calculated to be approximately 1.1 mm. This warm-up would occur at approximately 50 seconds into the atmospheric entry and last for about one minute. In the end, at landing, the temperature throughout the structure would be around 200 °C.

In *Small (mini) landing station systems tests* from 2002 is a description of thermal protection systems (the frontal area of the lander in MIBD configuration) tests and their results. Small sample plates of the used material were tested in a Hall accelerator. The heat fluxes used were based on calculation results. For example, the maximum heat flux would occur at the stagnation point in the frontal area and the heat flow would reach, according to the documentation, approximately 450 $\frac{\mathrm{kW}}{\mathrm{m}^2}$. Eight different samples were then subjected to various heat fluxes for a time period of 38 ± 0.5 seconds. The results show that the external layer reached 510 °C and the temperature of the internal layer did not exceed 220 °C [22].

2.5.3 Drop tests

In order to determine the forces and accelerations during the impact into the Martian surface, drop tests were performed by LA. The design impact speed is 60 $\frac{\mathrm{m}}{\mathrm{s}}$ and the mass of the penetrating part is 5.02 kg. With this initial data, calculations have again been performed for the vehicle as well as full-scale model drop tests. In these tests, the inclination angle was varied between 0 and 30 degrees. The soil models used in the calculations were granular (sandy), average density (clay) and rock.

The calculation results were documented as graphs of g-load and sequences of images portraying the penetrating phase. They indicate that the maximum g-load is approximately 500, which appears when the horizontal speed is 15 $\frac{\mathrm{m}}{\mathrm{s}}$ and inclination is 30 degrees (granular soil). Travel depth into the soil reached a maximum of 230 mm. [5]

Full-scale drop tests were also described in the documentation. Two lander modules were used for the tests: a dynamic model with properties close to the actual vehicle; and an overall-mass model for the verification of test conditions and methodology. Two soil models were used here: sandy and firm soil. [23]

The documentation does not provide any results from the drop tests. Therefore, the only conclusion that can be drawn from these documents is that landing speed should not exceed 60 $\frac{\mathrm{m}}{\mathrm{s}}$.

Chapter 3

Theoretical background

In this chapter we take a theoretical look of the MetNet landing vehicle, define the pertinent terms and quantities and finally introduce requirements for it. Even though the geometry is far different from traditional airplanes, general aeronautical definitions can be applied to the vehicle. The applicable quantities are calculated in order to assess the qualities of the vehicle.

3.1 Aerodynamics of the vehicle

Like any object, the MetNet lander disturbs the medium around it when flying through the Martian atmosphere. The molecules colliding into the object change their direction, causing a momentum change in the flow. For example, if the vehicle is advancing slightly turned in relation to the incoming flow, some particles will pass it from over the vehicle and some under the vehicle. Due to the asymmetry of the geometries experienced by the particles, they will attain different speeds and pressures. In short, the process is similar to the effects that cause lift and drag force in airplane wings.

In order to describe and calculate the pertinent aerodynamic quantities for the vehicle, a coordinate system will have to be defined. The origin is located wherever it is defined when the calculation mesh is created. In the cases created in this work, the origin is set to the nose or tip of the vehicle. The x-axis needs to be consistent with FINFLO: the positive x-axis is the flow direction (if the angle of attack is zero). Note that this is the inverse of what was implied in Figure 2.7. See Figure 3.1 for the coordinate definitions in FINFLO. The y- and z-axes form the right-handed coordinate system with the x-axis. Note also that due to the rotational symmetry of the vehicle, the actual directions of the y- and z-axes remain vague. However, in the mesh creation, the xy-plane is defined as the symmetry plane. The direction

vectors $\vec{i}$, $\vec{j}$ and $\vec{k}$ are defined to be unit vectors in the directions of x-, y-, and z-axis, respectively. The surface domain of the vehicle (thought as rigid and smooth) is denoted by A and $\vec{n}$ is the normal vector at each point, pointing outwards from the vehicle.

In FINFLO, the angle of attack is varied by changing the direction of the incoming flow (not by rotating the vehicle) and thus the angle of attack does not affect the orientation of the vehicle in the coordinate system. The angle of attack α is, therefore, defined as the angle between the x-axis and the incoming flow (in the symmetry plane or the xy-plane), so that rotation along positive z-axis is considered positive. It would also be possible to define the sideslip angle β, but it would not contribute to this work due to symmetry.

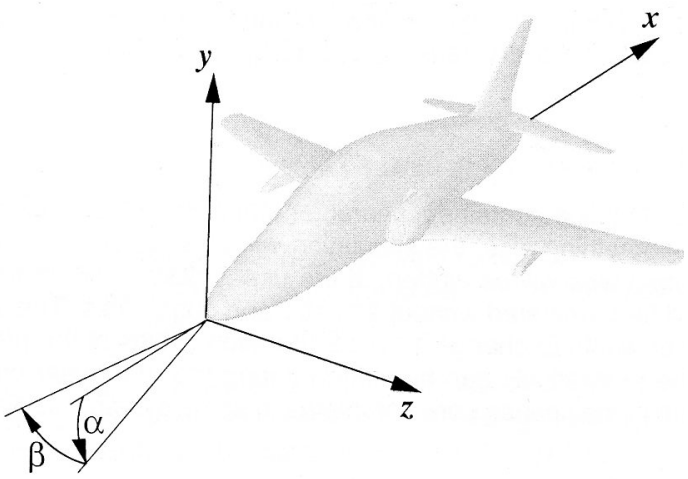

Figure 3.1: Coordinate system definitions in FINFLO [24].

The interaction between the vehicle and the medium around it creates forces that act on the vehicle. Normally there would be three force components and three moment components, but since the cases in this work have rotational symmetry, we can manage with two force components and one moment component. The two force components are the forces in the direction of $\vec{i}$- and $\vec{j}$-vectors and are called the normal force and the axial force, respectively. The third force component, for a more general geometry, would have been the side force, defined in the z-direction.

The moment needed in the examination of the aerodynamics of the vehicle is the pitching moment, defined in the direction of negative z-axis (positive when turning the nose up or increasing the angle of attack). The missing moments would be the rolling moment, which is defined in the direction of

negative x-axis, and the yawing moment, defined in the direction of negative y-axis. Again, the two latter moments disappear due to symmetry.

D.F. Kurtulus has formulated, using momentum balance, a general equation for the calculation of the aerodynamic forces on an arbitrary shape immersed in a fluid [25]. For the stationary case, the axial and normal forces become

$$\begin{aligned} \vec{F}_A &= \iint_A \left[-\rho \left(\vec{U} \cdot \vec{n} \right) \vec{U} + p\vec{n} - \bar{\bar{\tau}} \cdot \vec{n} \right] \cdot \vec{i} \, \mathrm{d}S \\ \vec{F}_N &= \iint_A \left[-\rho \left(\vec{U} \cdot \vec{n} \right) \vec{U} + p\vec{n} - \bar{\bar{\tau}} \cdot \vec{n} \right] \cdot \vec{j} \, \mathrm{d}S \end{aligned} \tag{3.1}$$

where $\vec{U}$ is the local velocity vector and $\bar{\bar{\tau}}$ is the viscous stress tensor. In practise, the terms in Equation 3.1 are obtained from momentum fluxes. The components of the viscous tensor are

$$\tau_{i,j} = \tau_{j,i} = \mu \left[\frac{\partial u_j}{\partial x_i} + \frac{\partial u_i}{\partial x_j} - \frac{\partial u_k}{\partial x_k} \delta_{i,j} \right] - \left(\overline{\rho u_i'' u_j''} - \delta_{i,j} \frac{2}{3} \rho k \right) \tag{3.2}$$

In this notation, u_i represent the three velocity components and x_i represent the coordinates, k is turbulence kinetic energy, $\delta_{i,j}$ is the Kronecker delta, and $\overline{\rho u_i'' u_j''}$ is the Reynolds stress. These terms will be discussed in Chapter 5. The pitching moment about an arbitrary point P of the vehicle is then

$$\vec{M}_P = \iint_A \left(\left[\rho \left(\vec{U} \cdot \vec{n} \right) \vec{U} + p\vec{n} - \bar{\bar{\tau}} \cdot \vec{n} \right] \times \vec{r} \right) \cdot \vec{k} \, \mathrm{d}S \tag{3.3}$$

where $\vec{r}$ is the distance from the reference point to the integration point. Another way of presenting these quantities is the coefficient form

$$\begin{cases} F_N = C_N \frac{1}{2} \rho U^2 S \\ F_A = C_A \frac{1}{2} \rho U^2 S \\ M = \left| \vec{M} \right| = C_m \frac{1}{2} \rho U^2 S \bar{c} \end{cases} \tag{3.4}$$

here C_N, C_A and C_m are the normal, the axial and the moment coefficient about the centre of mass, respectively; ρ is the medium density, U is the free stream velocity, S is the reference area, and $\bar{c}$ is the reference length. In the case of the MetNet lander, we can set the reference length to be the largest diameter of a given geometry ($\bar{c} = 1$ m for the MIBD case and $\bar{c} = 2$ m for the AIBD case) and the area to be the cross-sectional area at the point of the largest diameter, resulting in $S = \frac{\pi}{4} \bar{c}^2$.

The aerodynamic coefficients C_A, C_N and C_m are in the centre of attention in this work. They can be thought of as the aerodynamic characteristics of the vehicle. With them, it is possible to make calculations about the behaviour of the vehicle when it is advancing in the medium. They depend strongly on the angle of attack of the vehicle and the Mach and Reynolds numbers. However, a more common form for the force coefficients is the use of lift and drag coefficients C_L and C_D, coefficients for forces relative to the outside environment and not the vehicle. They can be easily calculated from the axial and normal coefficients from Equation (2.15). These are the coefficients that FINFLO is able to calculate, alongside the moment coefficient.

The pitching moment coefficient about the centre of mass C_m is also of great importance in this work. Two derivative terms can be defined from it:

- $C_{m_\alpha} = \frac{\partial C_m}{\partial \alpha}$ is the variation of the pitching moment coefficient with the angle of attack or slope of pitching moment coefficient the with respect to the angle of attack. Here it is assumed that pitching moment coefficient varies approximately linearly with the angle of attack. In reality, approximate values are calculated for this term so that $C_{m_\alpha} \approx \frac{\Delta C_m}{\Delta \alpha}$. The derivative is approximated by difference terms. Thus the value for this coefficient can be approximately computed if the pitching moment coefficient is calculated for several angles of attack.

- The slope of pitching moment coefficient with respect to the pitch rate $C_{m_q} = \frac{\mathrm{d}C_m}{\mathrm{d}\left(\frac{\dot{\alpha}\bar{c}}{2U}\right)}$, where q is the pitch rate or the angular rate of the vehicle around the z-axis. Due to rotational symmetry, in this work it can be equated to the time derivative of the angle of attack, $q = \frac{\mathrm{d}\alpha}{\mathrm{d}t} = \dot{\alpha}$. Note that the so called normalization is carried out in the differentiation in order to give sensible units for the derivative and to make it independent of free flow speed. Computing a value for this coefficient would require forcing the angle of attack to oscillate at different frequencies and then compute how much the pitching moment coefficient is affected by that frequency. This would require very extensive computations and is not calculated in this work.

It should be noted that in this work the cross-section of the vehicle is approximated as a perfect circle. In reality, the realised geometry will be, for the solid parts, as close to a circle as it is possible to fabricate, but the inflatable parts will actually form a 12-gon. Now a question arises: can the 12-gon be approximated as a circle in the context of this work? The area of a regular 12-gon is, omitting the proof, exactly 3 times the outer radius squared. Thus the ratio of the areas, when we think of a circle and a 12-gon superimposed, is $^3/_\pi \approx 0.9549$. Since the aerodynamic forces are directly

proportional to the cross-sectional area, we can conclude that the error in the aerodynamic coefficients between a 12-gon and a circle is less than 5 per cent. This is an acceptable error and thus we can from now on approximate the cross sections as circles.

3.2 Aerodynamic stability of the vehicle

As already discussed in Section 2.4, the vehicle must be designed so that it stays upright during the descent stage. In other words, the angle of attack must remain constrained. This is equivalent to the aerodynamic stability of the vehicle and it can be divided into two parts: static and dynamic stability. A general definition for static stability is provided by Roskam [26]:

> Static stability is defined as the tendency of an airplane to develop forces or moments which directly oppose an instantaneous perturbation of a motion variable from a steady-state flight condition.

A definition for dynamic stability is also provided by Roskam:

> Dynamic stability is defined as the tendency of the amplitudes of the perturbed motion of an airplane to decrease to zero or to values corresponding to a new steady state at some time after the cause of the disturbance has stopped.

In order to use the definition of static stability in the context of this work, we will interpret "steady-state flight condition" as a flight condition where the angle of attack is constant. A "perturbation" would then mean any change in angle of attack from this constant value. If the vehicle is statically stable, it would then, according to the first definition, develop forces and moments that oppose this change. For example, if the steady-state value for the angle of attack is zero and some perturbation occurs so that the angle of attack becomes positive, the aerodynamic effects would tend to decrease this value back to zero and the pitching moment would be negative.

The definition of dynamic stability concerns the amplitude of the perturbed motion variable and is fulfilled if the amplitude diminishes to zero. Simulations of these phenomena require time accurate simulations that would take several orders of magnitude more calculation time (see the previous subsection). In this work, such simulations are not run, but as computers become faster and faster it is imaginable that some day these simulations could be done.

The orientation of the vehicle in relation to the incoming flow can completely be defined with the angle of attack (α) alone and it is the only motion

variable in the model related to the orientation. This is due to the previously discussed rotational symmetry. Other motion variables that could be discussed would be the velocities of the vehicle along different coordinates (x and y), and one could discuss the stability for these variables as well. Other kinds of stability would not be important in the design of the vehicle since, for example, it is specifically desirable that the vehicle slows itself down as much as possible. The evolution of velocity variables are treated in the trajectory calculations in Chapter 4.

3.3 Stability criterion for the vehicle

In order to approach the stability of the vehicle from a mathematical point of view, an equation of motion must be developed. As mentioned, the only motion variable of interest in the stability analysis is the angle of attack α and the aerodynamic stability of the vehicle is thus related to its evolutions with time. Newton's second law applied for rotational systems states that the net moment applied to a body is proportional to the angular acceleration it obtains:

$$\sum M_z = I_z \frac{\mathrm{d}^2\alpha}{\mathrm{d}t^2} \tag{3.5}$$

Rotation is interpreted here as the change of angle of attack α. Thus the moments are calculated around the z-axis. The only moment applied to the body is the aerodynamic moment around the z-axis. Next, we will make a Taylor-type approximation for the moment:

$$M_z \approx M_z(\alpha = 0) + \frac{\mathrm{d}M_z}{\mathrm{d}\alpha}\alpha + \frac{\mathrm{d}M_z}{\mathrm{d}\left(\frac{\dot{\alpha}\bar{c}}{2U}\right)}\frac{\dot{\alpha}\bar{c}}{2U} \tag{3.6}$$

Here $\dot{\alpha} = \frac{\mathrm{d}\alpha}{\mathrm{d}t} = q$ is the pitch rate or the time derivative of the angle of attack. This quantity can be thought as analogous to angular velocity. Additionally we can assume $M_z(\alpha = 0) = 0$ considering the vehicle as symmetric. The pitch rate term has already been discussed in Section 3.1. Now the coefficient forms from Equation (3.4) can be used:

$$M_z \approx \frac{\mathrm{d}C_m}{\mathrm{d}\alpha}\alpha\frac{1}{2}\rho U^2 S\bar{c} + \frac{\mathrm{d}C_m}{\mathrm{d}\left(\frac{\dot{\alpha}\bar{c}}{2U}\right)}\frac{\dot{\alpha}\bar{c}}{2U}\frac{1}{2}\rho U^2 S\bar{c} = C_{m_\alpha} q_\infty S\bar{c}\alpha + C_{m_q}\frac{q_\infty S\bar{c}^2}{2U}\dot{\alpha} \tag{3.7}$$

Here the dynamic pressure is $\frac{1}{2}\rho U^2 = q_\infty$. With this result and Newton's second law, we obtain the differential equation of the angular movement for the MetNet lander:

$$I_z\ddot{\alpha} - \frac{q_\infty S\bar{c}^2}{2U}C_{m_q}\dot{\alpha} - q_\infty S\bar{c}C_{m_\alpha}\alpha = 0 \tag{3.8}$$

Equation (3.8) is a homogenic second-order linear ordinary differential equation corresponding to an equation of harmonic motion with damping. The solution of this equation involves the use of a characteristic equation and its roots. Omitting the calculation steps, the roots of the characteristic equation are

$$\lambda_{1,2} = \frac{1}{2}\left(\frac{q_\infty S\bar{c}^2}{2UI_z}C_{m_q} \pm \sqrt{\left(-\frac{q_\infty S\bar{c}^2}{2UI_z}C_{m_q}\right)^2 + 4\frac{q_\infty S\bar{c}}{I_z}C_{m_\alpha}}\right) \tag{3.9}$$

It can be shown that the solutions for Equation (3.8) are stable (the amplitudes of the oscillations will tend to zero as time increases) if and only if the real parts of both of the roots are negative. For this next part only, let us make a shorthand notation $-\frac{q_\infty S\bar{c}^2}{UI_z}C_{m_q} = a$ and $-\frac{q_\infty S\bar{c}}{I_z}C_{m_\alpha} = b$. Since all the quantities are real numbers, this condition becomes

- If $a^2 - 4b \geq 0$ ($\Leftrightarrow \lambda_{1,2} \in \mathbb{R}$), the plus-signed condition yields $a > \sqrt{a^2 - 4b} \geq 0 \Rightarrow a > 0$ and $a^2 > a^2 - 4b \Rightarrow b > 0$ or $a, b > 0$. The condition for the minus-signed root is automatically fulfilled.
- or, if $a^2 - 4b < 0 \Rightarrow \lambda_{1,2} = \frac{1}{2}\left(-a \pm i\sqrt{4b - a^2}\right)$ where $i^2 = -1$ and $\mathrm{Re}(\lambda_{1,2}) = -\frac{a}{2} < 0 \Rightarrow a > 0$ and $a \in \mathbb{R} \Rightarrow b > \frac{a^2}{4} > 0$.

Recognising that all the other quantities are positive, the stability condition becomes $a, b > 0$ or $C_{m_\alpha} < 0$ and $C_{m_q} < 0$. This is an intuitive result: a negative slope for the pitching moment coefficient means that the pitching moment obtains negative values when α is positive, thus creating a moment that opposes the perturbation from zero angle of attack. A negative value for the slope of the pitching moment with the pitch rate means that an increase in the speed at which a (positive) angle of attack grows increases the opposing (negative) pitching moment, thus damping the oscillations. The C_{m_q} term is, therefore, sometimes called the damping derivative.

Chapter 4

Calculation of landing trajectory

In order to calculate the trajectories for the lander, a set of differential equations is used. The equations, derived by J.C. Adams [27], describe the motion of a generic lander vehicle with derivative terms where the variable of differentiation is either time or altitude. Naturally, the solutions for these two should be equal. There is, however, a discrepancy between the two sets of equations: the time derivatives are dependent of the lift-to-drag ratio of the vehicle while the altitude derivatives are not.

The original equations as presented by Adams are:

$$\begin{cases} \dfrac{dU}{dh} = \dfrac{g\left[\frac{q_\infty}{\beta_w} - \sin\gamma\right]}{U\sin\gamma} \\ \dfrac{d\gamma}{dh} = \dfrac{\cos\gamma\left[-g + \frac{U^2}{R_m+h}\right]}{U^2\sin\gamma} \\ \dfrac{dt}{dh} = \dfrac{-1}{U\sin\gamma} \\ \dfrac{dr}{dh} = \dfrac{-R_m\cos\gamma}{(R_m+h)\sin\gamma} \end{cases} \tag{4.1}$$

and

$$\begin{cases} \dfrac{dU}{dt} = g\left[\dfrac{-q_\infty}{\beta_w} + \sin\gamma\right] \\ \dfrac{d\gamma}{dt} = \dfrac{-\frac{q_\infty g}{\beta_w}\frac{L}{D} + \cos\gamma\left[g - \frac{U^2}{R_m+h}\right]}{U} \\ \dfrac{dh}{dt} = -U\sin\gamma \\ \dfrac{dr}{dt} = \dfrac{R_m U\cos\gamma}{R_m+h} \end{cases} \tag{4.2}$$

where

- U is the vehicle velocity magnitude
- γ is the flight path angle in radians (positive below the horizontal ; $\frac{\pi}{2}$ would be "straight down")
- h is the altitude
- r is the flight range above the surface
- t is the flight time
- R_m is the radius of Mars ; $R_m \approx 3386$ km
- g is the acceleration of gravity; it can be calculated from $g(h) = g_m \left(\frac{R_m}{R_m+h}\right)^2$; $g_m \approx 3.71 \frac{\mathrm{m}}{\mathrm{s}^2}$ is the acceleration of gravity on the surface of Mars.
- $q_\infty = \frac{1}{2}\rho U^2$ is dynamic pressure at a given altitude. The density ρ can be calculated from Equation (2.10).
- β_w is the ballistic coefficient $\beta_w = \frac{W}{C_D A}$; $W = mg$ is the vehicle weight (in Newtons – notice this uncommon notation); C_D is the drag coefficient and A is the reference area used in the determination of drag coefficient. In our case $A = \frac{\pi}{4}D^2$ where D is the diameter of the vehicle. Although the ballistic coefficient is usually expressed as mass divided by the drag coefficient times reference area, here the choice of using the weight of the vehicle instead ensures that the units of the equations are consistent.
- $\frac{L}{D} = \frac{C_L}{C_D}$ is the lift-to-drag ratio of the vehicle.

The aforementioned discrepancy can be easily corrected using differential algebra. Since the term affected by the lift-to-drag ratio is γ, we can write

$$\frac{d\gamma}{dh} = \frac{d\gamma}{dt}\frac{dt}{dh} = \frac{-\frac{q_\infty g}{\beta_w}\frac{L}{D} + \cos\gamma[g - \frac{U^2}{R_m+h}]}{U}\frac{-1}{U\sin\gamma} = \frac{\frac{q_\infty g}{\beta_w}\frac{L}{D} + \cos\gamma[-g + \frac{U^2}{R_m+h}]}{U^2\sin\gamma}$$

This is the equation that will replace the term for $\frac{d\gamma}{dh}$ in Equation (4.1). The other equations are consistent.

Another noteworthy feature that can be seen from the equation set is that it is easy to solve the landing speed. It can be solved by setting $\frac{dU}{dt} = 0$ and solving U from that equation, resulting in

$$U_{\text{final}} = \sqrt{\frac{8W \sin\gamma}{C_D D^2 \rho \pi}} \tag{4.3}$$

Since the design landing speed is under 58 $\frac{\text{m}}{\text{s}}$, an expected (minimum) value for the drag coefficient for the AIBD case is

$$C_D \approx \frac{8 \times (13.81 \text{ kg})(3.71 \frac{\text{m}}{\text{s}^2})(\sin 90°)}{\pi(0.0164 \frac{\text{kg}}{\text{m}^3})(58 \frac{\text{m}}{\text{s}})^2(2 \text{ m})^2} \approx 0.59$$

The value for the density at landing was taken from the results in Subsection 2.2.4. Now the Reynolds number in landing is

$$\text{Re} = \frac{(0.0164 \frac{\text{kg}}{\text{m}^3})(58 \frac{\text{m}}{\text{s}})(2 \text{ m})}{1.92 \times 10^{-7} \frac{226^{1.8}}{226+60} \frac{\text{kg}}{\text{ms}}} \approx 160\,000$$

The given equations are a set of ordinary differential equations. Once the initial values of all the variables listed above are known, the successive values can be computed with a suitable method. In this case, the explicit first-order forward Euler method was chosen and a Python solver was created for the task.

The downside of the first-order Euler method is that a relatively small time step (or altitude step) has to be used. The results become more accurate when $\Delta t \to 0$. In practise a small enough step was chosen so that further diminishing did not significantly alter the results. Additionally, some dynamic changing of the time step was implemented into the code. This is because derivatives are highly dependent of γ. The derivatives are large if γ is small and a minuscule value for Δt has to be used. When γ is large (towards the end of the solution), it is safe to take a significantly larger step size.

4.1 Parameter value ranges

Several parameter values must be provided for FINFLO in order to run the simulations. For example, the combination of Reynolds number and Mach number must be given. Even before any FINFLO simulations, the trajectory calculations can provide the range of values for these parameters that the vehicle experiences. Therefore, a number of initial trajectory calculations are performed. The following assumptions are made:

- Vehicle mass is $m = 22$ kg for MIBD and $m = 13.81$ kg for AIBD.

- The reference area is $\frac{\pi}{4}$ m$^2 \approx 0.785$ m^2 for MIBD and π m$^2 \approx 3.14$ m^2 for AIBD.

- Entry velocity for MIBD is within 10 % of the nominal value; $U_{\text{entry}} = 4100 \ldots 5000$ $\frac{\text{m}}{\text{s}}$.

- Initial altitude for MIBD is 120 000 m.

- The entry angle for MIBD is $\gamma = 8 \ldots 20°$.

- The drag coefficient for MIBD is $C_D = 0.6 \ldots 1.4$ (see Figure 2.11). For AIBD, $C_D = 0.8 \ldots 1.2$, a range slightly larger than what was obtained before [15].

- The lift coefficient is zero for both cases. This is due to the assumption that the vehicle's angle of attack oscillates around zero throughout the flight and thus the average lift coefficient is close to zero. Moreover, since we want $\gamma = 90°$ at the end of the descent phase, the condition $\frac{d\gamma}{dt} = 0$ yields $-\frac{Qg}{\beta_w}\frac{L}{D} + \cos 90°[g - \frac{V^2}{R_m+h}] = 0 \Rightarrow \frac{L}{D} = 0 \Rightarrow C_L = 0$.

With these initial values and the atmospheric model provided in Section 2.2, eight different trajectories are calculated for the MIBD phase. See Table 4.1 for the naming convention. The results were filtered so that Kn < 0.2 and Ma ≥ 0.85. The following conclusions are drawn from the results for the MIBD phase:

- The possible Reynolds number values are Re $= 40\,000 \ldots 500\,000$, applicable to almost the whole range of Mach numbers. However, at very large Mach numbers, Reynolds number becomes very small, that is Re ≈ 200 when Ma $\gtrsim 25$.

- The Reynolds number achieved at the end of the MIBD phase (Ma $= 0.85$) are Re $= 100\,000 \ldots 300\,000$.

- The altitude at which Ma $= 0.85$ is achieved is in the range $2 \ldots 12$ km. The lower value is alarming, but it is achieved when $C_D = 0.6$, which is a very small value for the drag coefficient. Once the simulated value for the drag coefficient is known, a better trajectory calculation can be made.

- The trajectory angle at Ma $= 0.85$ is $\gamma \approx 50° \ldots 60°$.

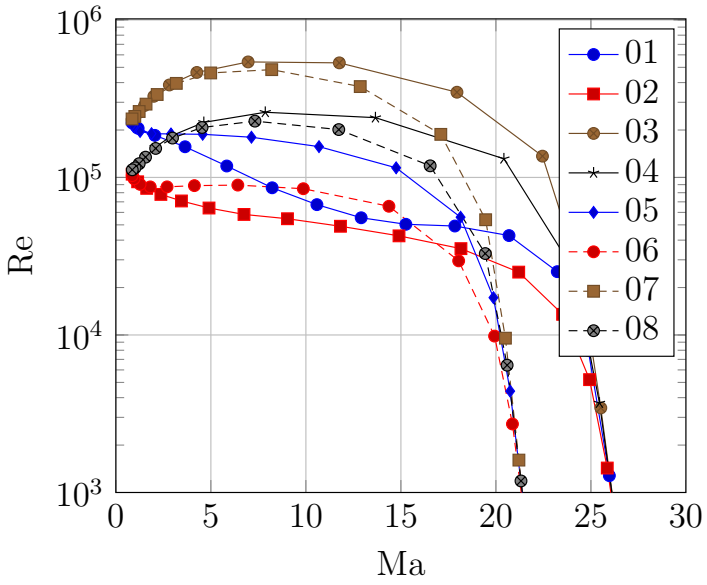

Figure 4.1: The ranges of Mach number versus Reynolds number for the eight different cases for the MIBD configuration (see Table 4.1). The end points of the curves correspond to the AIBD deployment point condition, Ma = 0.85.

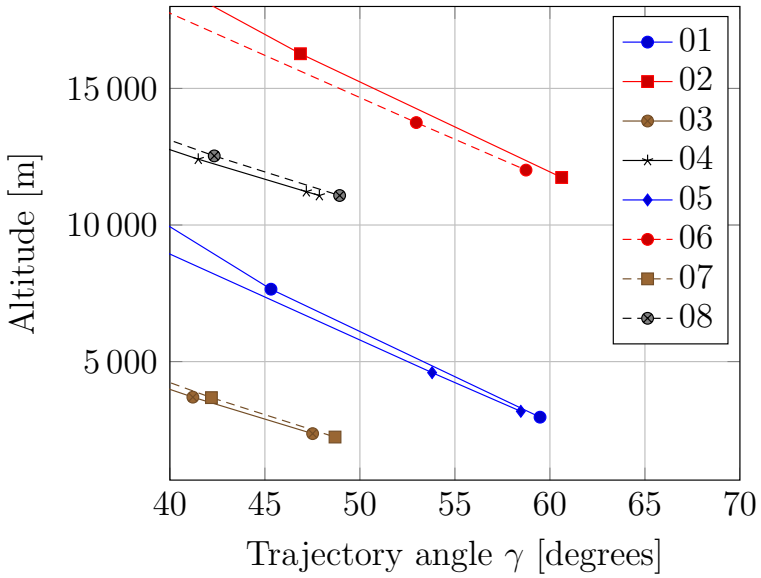

Figure 4.2: The ranges of trajectory angle γ versus altitude for the eight different cases for the MIBD configuration. The end points of the curves correspond to the AIBD deployment point, Ma = 0.85.

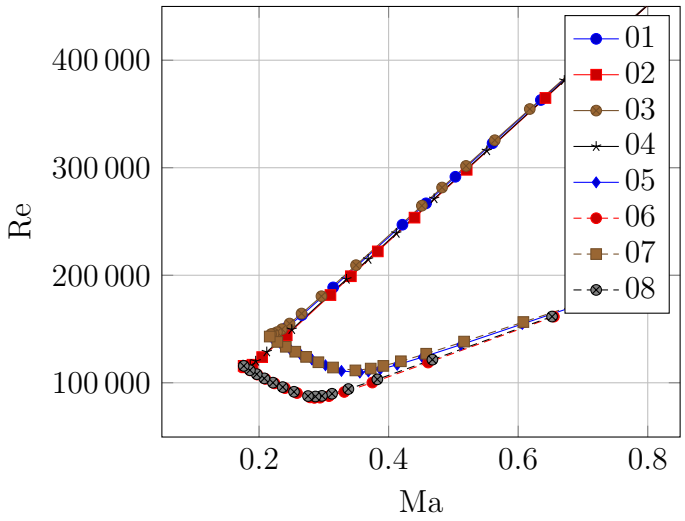

Figure 4.3: The range of Mach and Reynold numbers experienced by the AIBD phase according to the initial eight trajectory calculations. See Table 4.2 for the naming convention.

Since the values were duly filtered to match the MIBD case until AIBD deployment, the values at the end of the calculation (Ma = 0.85) can be used as initial values for new trajectory calculations for AIBD. Taking Ma = 0.85 and reading Figure 2.2, the airspeed of the vehicle at the AIBD deployment is $U \approx 200\ \frac{\mathrm{m}}{\mathrm{s}}$. This is used as the initial velocity for the trajectory calculation of AIBD. However, the vehicle slows down in between the two geometries: the MIBD separation time is non-zero and actually the vehicle will have been slowed down to Ma $= 0.45 \ldots 0.54$ when the AIBD configuration is deployed [4]. This is taken into account in the interpretation of the results.

Again, eight different cases were calculated. See Table 4.2 for the naming convention. The results for AIBD (see Figure 4.3) indicate that right after MIBD separation, the Reynolds number is Re $= 100\,000 \ldots 300\,000$. When the vehicle is closer to the ground and the Mach number is smaller, the values are Re $= 100\,000 \ldots 150\,000$. The Reynolds number ranges used in the simulations should thus be chosen accordingly.

Table 4.1: The naming convention for the initial trajectories of the MIBD configuration.

	$\gamma = 8°$		$\gamma = 20°$	
	$C_D = 0.6$	$C_D = 1.4$	$C_D = 0.6$	$C_D = 1.4$
$U_{\text{entry}} = 5\,000\ \frac{\text{m}}{\text{s}}$	Case 01	Case 02	Case 03	Case 04
$U_{\text{entry}} = 4\,100\ \frac{\text{m}}{\text{s}}$	Case 05	Case 06	Case 07	Case 08

Table 4.2: The naming convention for the initial trajectories of the AIBD configuration.

	$\gamma = 50°$		$\gamma = 60°$	
	$C_D = 0.8$	$C_D = 1.2$	$C_D = 0.8$	$C_D = 1.2$
$h = 2$ km	Case 01	Case 02	Case 03	Case 04
$h = 12$ km	Case 05	Case 06	Case 07	Case 08

4.2 Minimum entry angle for the atmospheric entry

If the entry angle is very small, it is possible that the vehicle bounces back to space and does not land on the planet at all. Therefore we define the minimum entry angle or the smallest entry angle γ_{init} whereby the vehicle reaches the ground. Heat loads could also impose limits for the entry angle, but in this portion we are only treating the trajectory calculations.

The code already developed for the trajectory calculations can be directly used to look for the minimum entry angle. It is not possible to formulate an analytical expression for the angle, since none of the Equations (4.1) directly corresponds to this case. Interpreting the trajectory equations, the cause for this is the combination of flight velocity and altitude. Since they cannot be directly connected with an equation, we must manage with numerical calculations. Due to the nature of the phenomenon, it is easy to implement a condition for this event: we simply stipulate that should the vehicle's altitude ever surpass the initial altitude, then it is considered as bounced back.

The starting point of these calculations is the ensemble of initial values already set in Section 4.1. It was observed that the minimum entry angle is virtually independent of the initial altitude and velocity, as long as they remain in the same order of magnitude as normally in the project (initial altitude $h_{\text{init}} = 120$ km, initial velocity $U_{\text{init}} = 4586\ \frac{\text{m}}{\text{s}}$). The only remaining value to be defined is the ballistic coefficient (in the traditional sense, where mass is used instead of weight). Let us denote this traditional ballistic coefficient by

$$\beta_m = \frac{m}{C_D S} \tag{4.4}$$

The results from LA indicate that this value could be approximately $\beta_m \approx 19 \ldots 22$ for the MetNet lander. It is now possible to calculate the minimum entry angles when the value of β_m is set. The results are in Table 4.3. For the MetNet case, it would be, therefore, sensible to limit the entry angle to angles greater than 6 degrees.

Table 4.3: The minimum entry angles to prevent bounce-back, for the MetNet case as a function of the traditional ballistic coefficient.

β_m	8	15	20	30	45	70	100	150	200
Minimum entry angle γ_{min}, degrees	5.25	5.65	5.83	6.07	6.31	6.55	6.75	6.96	7.11

Chapter 5

FINFLO Solver

5.1 Solution algorithm

In order to solve the quantities in the flow field, the so called Reynolds averaging process is used [28], where each quantity is decomposed into the time averaged part and the fluctuating part. Any flow quantity Q is then written as

$$Q(x,y,z,t) = \overline{Q(x,y,z)} + Q^{'}(x,y,z,t) \tag{5.1}$$

where $\overline{Q(x,y,z)}$ is the time averaged part and $Q^{'}(x,y,z,t)$ is the fluctuating part. When this technique is applied to the Navier-Stokes equations, the so called Reynolds-averaged Navier Stokes (RANS) equations are formed. These are the equations that FINFLO solves, and the FINFLO manual formulates this equation as [24]

$$\frac{\partial U}{\partial t} + \frac{\partial \left(F_i - F_{vi}\right)}{\partial u_i} = Q_s \tag{5.2}$$

where $U = (\rho, \rho u_1, \rho u_2, \rho u_3, E, \rho k, \rho \epsilon, \rho \phi)^T$ and Q_s is the source term. Einstein summation over i is implied in this equation. The terms u_i represent the flow velocities so that $\vec{U} = u_1\vec{i} + u_2\vec{j} + u_3\vec{k}$. The inviscid and viscid fluxes are solved separately, and the inviscid fluxes are solved with Roe's flux difference splitting method. This can be also modified by the user. The inviscid terms F_i are

$$F_i = \begin{pmatrix} \rho u_i \\ \rho u_1 u_i + \delta_{i,1}\left(p + \frac{2}{3}\rho k\right) \\ \rho u_2 u_i + \delta_{i,2}\left(p + \frac{2}{3}\rho k\right) \\ \rho u_3 u_i + \delta_{i,3}\left(p + \frac{2}{3}\rho k\right) \\ (E + p + \frac{2}{3}\rho k)u_i \\ \rho u_i k \\ \rho u_i \epsilon \\ \rho u_i \phi \end{pmatrix} \tag{5.3}$$

where E is the total internal energy, ϵ is turbulent dissipation, and ϕ is "a scalar variable describing, eg. the concentration of a species or the mass fraction of species". The viscous fluxes in Equation (5.2) are

$$F_{vi} = \begin{pmatrix} 0 \\ \tau_{1i} \\ \tau_{2i} \\ \tau_{3i} \\ u_j \tau_{ij} - q_i \\ \mu_k \left(\partial k / \partial x_i\right) \\ \mu_\epsilon \left(\partial \epsilon / \partial x_i\right) \\ \mu_\phi \left(\partial \phi / \partial x_i\right) \end{pmatrix} \tag{5.4}$$

where the Reynolds stress tensor components $\tau_{i,j}$ are defined in Equation (3.2), q_i are the heat fluxes, and μ_k, μ_ϵ and μ_ϕ are the diffusion coefficients of turbulence. The Einstein summation over j is implied in Equation (5.4).

Equation (5.2) can be solved numerically when the solution domain is discretised with the generated calculation mesh. There are several options for the numerical derivative discretisation scheme, including the first-order upwind, central, and second-order upwind schemes. The derivative terms are thus approximated as constants in each cell. Once the finite-volume technique is applied, Equation (5.2) can be integrated over the volumes and surfaces, and the Gaussian divergence theorem yields the following equation for a computational cell i:

$$V_i \frac{dU_i}{dt} = \sum_{\text{faces}} \left(-S_{\text{cell}} \hat{F} + V_i Q_i\right) \tag{5.5}$$

where V_i is the volume of the computation cell, $\hat{F} = n_j F_j$ is the flux through a face, n_j are the surface unit normals, S_{cell} is the surface area, and Q_i is the flux term in the cell. After this phase, the equations are rearranged in a matrix form so that

$$[\text{System matrix}]\,\{\Delta(\text{Quantities})\} = \{\text{Residuals}\} \tag{5.6}$$

If a density-based solution method is used in FINFLO, the DADI factorisation is applied to the system matrix. The residuals in the equation represent the implicit part of the system of equations, and therefore iteration of these equations has to be carried out. In the previous equation, Δ represents the change of quantities between iteration cycles. All the quantities can be considered solved if they change very little between iteration cycles. In other words, it is desirable that the residuals diminish as the number of iteration cycles grows. It is also possible to follow the evolution of residuals in real time during the calculation by calculating the L^2 (Eucledian) norm of the residual quantity in the Convergence program. See Figure 5.1 for an example graph of this evolution.

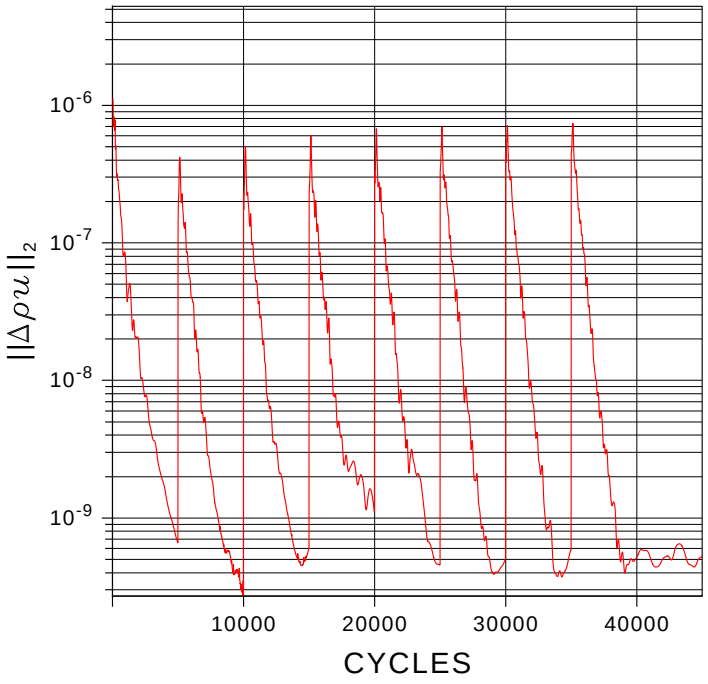

Figure 5.1: An example of residual diminuation for the MIBD case in a FINFLO simulation. The angle of attack was changed every 5 000 iterations, resulting in convergence between the different angles of attack. The graph was created with the FINFLO tool Convergence.

5.2 Turbulence model

When the Reynolds averaging process, discussed in the previous section, is carried out, terms called the Reynolds stresses (written as $\overline{u_i'' u_j''}$) occur in the equations. These terms can be thought as the turbulence terms and they need to be modelled.

The turbulence model of choice in this work is the Shear-Stress Transport (SST) k-ω-model, which belongs to the class of two-equation turbulence energy equation models. The idea behind the chosen model is to predict turbulence by introducing two parameters, k (turbulence kinetic energy) and ω (specific rate of dissipation of the turbulence kinetic energy), and then solving two partial differential equations for them [29]. This model has well proven its capabilities in the past decades and it can be thought as a combination of the k-ϵ and k-ω-models. This is because the latter is used in the boundary layers and the former in the free stream zones [30]. In order to ensure proper model selection, a blending function is used which operates as a function of the distance from the nearest wall. In FINFLO, two boundary condition values need to be specified by the user, which are the minimum value for ω and the free stream value of k. Also, the dimensionless turbulent viscosity can be limited with a maximum value. With these closure coefficients, the iteration cycle can be initiated.

The two equations are traditionally written as follows:

$$\begin{cases} \dfrac{\partial(\rho k)}{\partial t} + \dfrac{\partial(\rho u_j k)}{\partial x_j} = & P - \beta^* \rho \omega k + \frac{\partial}{\partial x_j}\left[(\mu + \sigma_k \mu_T)\frac{\partial k}{\partial x_j}\right] \\ \dfrac{\partial(\rho \omega)}{\partial t} + \dfrac{\partial(\rho u_j \omega)}{\partial x_j} = & \gamma \frac{\rho}{\mu_T} P - \beta \rho \omega^2 + \frac{\partial}{\partial x_j}\left[(\mu + \sigma_\omega \mu_T)\frac{\partial \omega}{\partial x_j}\right] \\ & +2(1-F_1)\frac{\rho \sigma_{\omega 2}}{\omega}\frac{\partial k}{\partial x_j}\frac{\partial \omega}{\partial x_j} \end{cases}, \tag{5.7}$$

where P is the production of kinetic energy, defined by

$$P = \overline{\rho u_i'' u_j''}\frac{\partial u_i}{\partial x_j} \tag{5.8}$$

μ_T is the turbulent eddy viscosity, calculated from

$$\mu_T = \frac{\rho a_1 k}{\max(a_1 \omega, S F_2)} \tag{5.9}$$

and the constant values can be seen in Table 5.1. The auxiliary coefficients γ_1 and γ_2 are

$$\begin{cases} \gamma_1 = & \dfrac{\beta_1}{\beta^*} - \dfrac{\sigma_{\omega 1} k^2}{\sqrt{\beta^*}} \\ \gamma_2 = & \dfrac{\beta_2}{\beta^*} - \dfrac{\sigma_{\omega 2} k^2}{\sqrt{\beta^*}} \end{cases} \tag{5.10}$$

Table 5.1: Coefficient values in the SST k-ω turbulence model [31].

Coefficient	β^*	σ_{k1}	σ_{k2}	$\sigma_{\omega1}$	$\sigma_{\omega2}$	β_1	β_2	a_1
Value	0.09	0.44	1	0.85	0.856	0.5	0.0828	0.31

The blending functions are

$$\begin{cases} F_1 = & \tanh\left\{\left[\min\left(\max\left(\dfrac{\sqrt{k}}{\beta^*\omega y}, \dfrac{500\mu}{\rho y^2\omega}\right), \dfrac{4\rho\sigma_{\omega2}k}{CD_{k\omega}y^2}\right)\right]^4\right\} \\ F_2 = & \tanh\left\{\left[\max\left(2\dfrac{\sqrt{k}}{\beta^*\omega y}, \dfrac{500\mu}{\rho y^2\omega}\right)\right]^2\right\} \end{cases} \tag{5.11}$$

where

$$CD_{k\omega} = \max\left(\frac{2\rho\sigma_{\omega2}}{\omega}\frac{\partial k}{\partial x_i}\frac{\partial\omega}{\partial x_i}, 10^{-10}\right) \tag{5.12}$$

The term S is related to the mean strain-rate tensor:

$$S = \sqrt{s_{i,j}s_{j,i}} \qquad \text{where} \qquad s_{i,j} = \frac{1}{2}\left(\frac{\partial u_i}{\partial u_j} + \frac{\partial u_j}{\partial x_i}\right) \tag{5.13}$$

Finally, the Reynolds stresses are calculated with the Boussinesq approximation [24] (compare with Equation 3.2)

$$-\overline{\rho u_i'' u_j''} = \mu_T\left[\frac{\partial u_j}{\partial x_i} + \frac{\partial u_i}{\partial x_j} - \frac{2}{3}\frac{\partial u_k}{\partial x_k}\delta_{i,j}\right] - \frac{2}{3}\rho k\delta_{i,j} \tag{5.14}$$

Chapter 6

Simulations

6.1 Simulation setup

6.1.1 Mesh Resolution

In order to correctly build the grid for the cases to be simulated, we need to first calculate the requirement for the height of the first mesh cell, here to be denoted by Δs, required to achieve a desired y^+, the dimensionless distance from the wall, using flat-plate boundary layer theory. The condition for this is

$$\Delta s = \frac{y^+ \mu}{U_\tau \rho} \tag{6.1}$$

The friction velocity, here denoted by U_τ, for a wall can be calculated from [32]

$$U_\tau = \sqrt{\frac{\tau_{\text{wall}}}{\rho}}, \tag{6.2}$$

where τ_{wall} is the wall shear stress. It can be calculated as

$$\tau_{\text{wall}} = c_f \frac{1}{2} \rho U^2 \tag{6.3}$$

Here U is the free stream velocity and c_f is the friction coefficient. White [32] provides an approximation for the friction coefficient for the case of a turbulent boundary layer:

$$c_f \approx \frac{0.027}{\text{Re}_x^{1/7}} \tag{6.4}$$

Here Re_x is the Reynolds number referred to the distance from the leading edge in the case of an airfoil. We can adopt this to our case by setting x

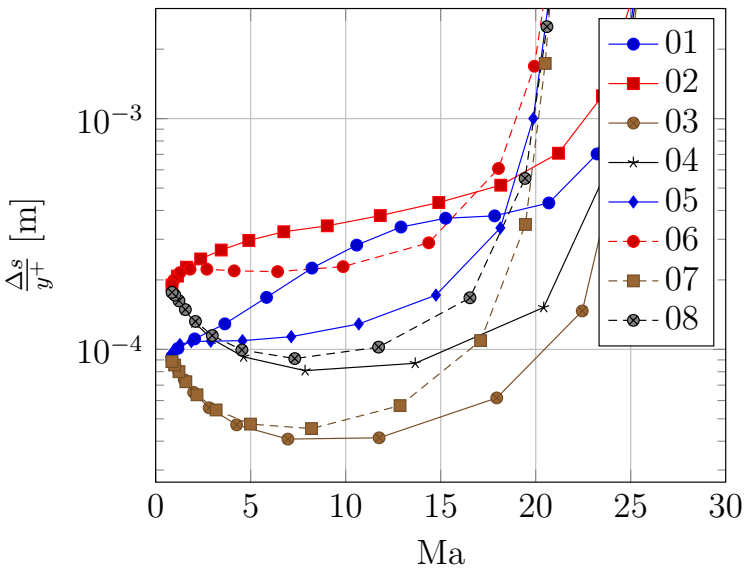

Figure 6.1: Calculated values for the ratio $\frac{\Delta s}{y+}$ as a function of Mach number for the MIBD case. The trajectory values for eight different cases were used from Section 4.1.

to be the reference length of each of the cases, that is the diameter of the lander.

Since the SST k-ω turbulence model is used, the appropriate value for the dimensionless wall distance is $y^+ = 1$. The values for Δs can now be calculated for each case, based on the other parameter values for each case. Since the results depend on the trajectory, the results calculated in Section 4.1 are used. Since they were calculated with a spreadsheet, it is easy to implement Equations (6.1) through (6.4) and thus calculate the value of Δs for each of the 16 cases.

The results of calculating the height of the first cell (See Figures 6.1 and 6.2) Δs indicate that

- For the MIBD case, the minimum Δs occurring is $\Delta s \approx 0.00004$ m, applicable to a wide range of Mach numbers.
- For the AIBD case, the Δs that should be used is $\Delta s \approx 0.00010$ m.

6.1.2 Mesh generation and boundary conditions

The calculation mesh for the MIBD case was generated with the Gridgen software [33], using a CAD file obtained from FMI. The model differs slightly

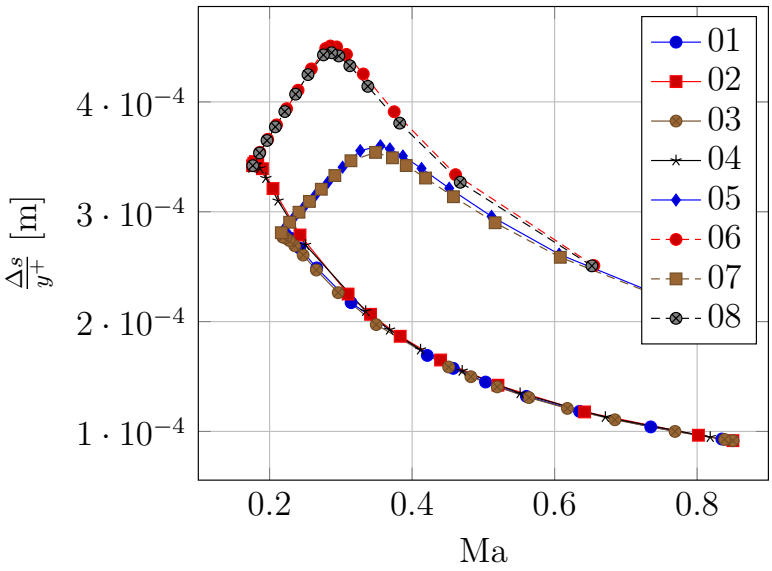

Figure 6.2: Calculated values for the ratio $\frac{\Delta s}{y+}$ as a function of Mach number for the AIBD case. The trajectory values for the eight different cases were used from Section 4.1.

from that portrayed in Figure 2.7. The model provided by LA, which was used in the creation of the grid, can be seen in Figure 6.3. Notice that the diameter (and the reference length) of the model is 1014 mm. Thus the reference area of the MIBD case in the simulations, taking into account that only half of it is modeled, is $\frac{\pi}{8}(1.014 \text{ m})^2 \approx 0.4038 \text{ m}^2$. Additionally, a scaling factor of 10^{-3} was applied to the grid in order to ensure proper units (metres).

Since the vehicle has rotational symmetry, only a 180° rotation of a 2D-slice had to be done. A total of 411 node points was created along the edge of the other half of the vehicle's 2D slice. The distance between the nodes was approximately 4.2 mm. These were then extruded outwards from the surface by 193 nodes. The height of the first cell was the default value, $\Delta s = 10^{-5}$ m (see the previous subsection). The node growth rate was initially 1.075 and was raised to the recommended upper limit, 1.20, as the distance from the vehicle grew larger. The final diameter of the thus created semi-circle is approximately 83.5 m, much larger than the diameter of the vehicle. This semi-circle was then rotated 180° around the x-axis, adding 97 nodes in the rotational direction. At this point, the grid was not still usable due to the singularities at the rotational axes. These were replaced with another blocks that were created with the Assemble Faces-tool instead of the Extrude-tool. The total number of cells was then 7 077 888, see Figure 6.4. A coarser

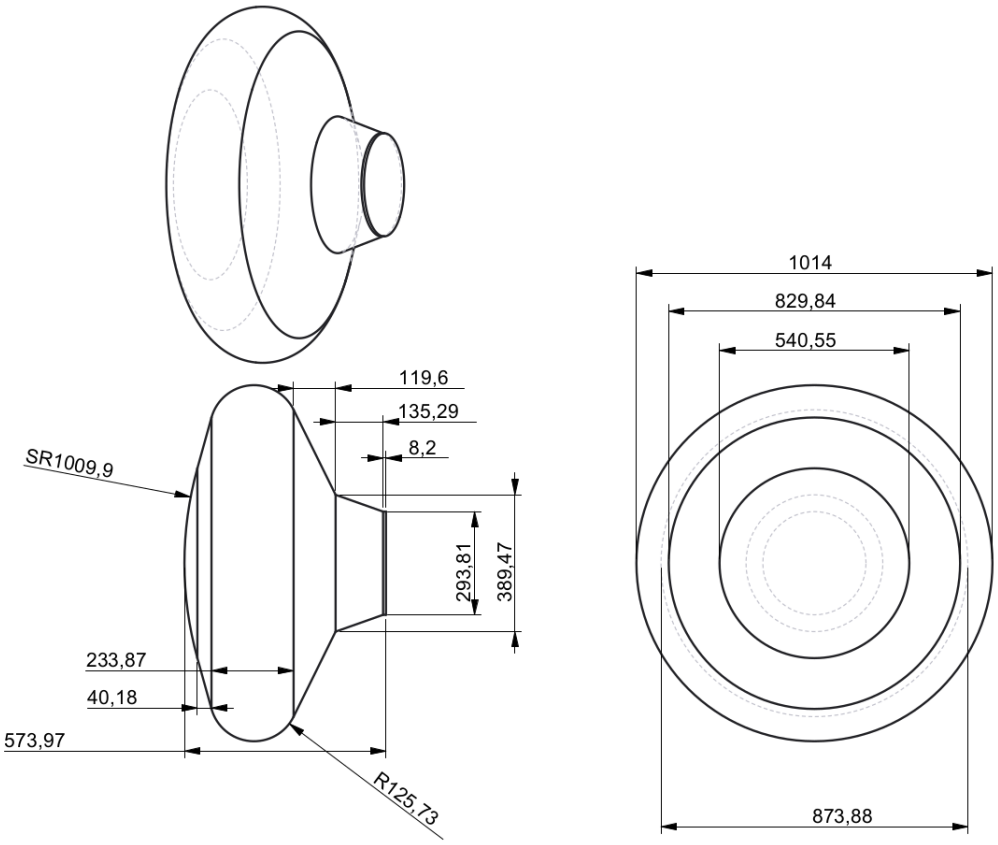

Figure 6.3: The CAD model used in the creation of the MIBD case mesh.

mesh with roughly 1.4 million cells was also created in order to see how the meshing density affects the results.

The same approach was used in the creation of the calculation mesh for the AIBD case. Again, the model differs slightly from what can be seen in Figure 2.9. The biggest difference is that the diameter is 1 800 mm instead of 2 000 mm, giving a reference area of $\frac{\pi}{8}(1.8\text{ m})^2 \approx 1.272\text{ m}^2$ for the simulations.

The number of nodes defined in the xy- plane was 181, giving distances ranging from 2.4×10^{-4} m to 4.5×10^{-2} m between nodes. The surface nodes were then extruded out by 101 nodes. The largest height of the first cell was $\Delta s = 0.0003$ m. The diameter of the thus created 2D grid is then approximately 51 m. The grid was again rotated 180 degrees, adding another 101 nodes in the rotational direction. The singularities were again removed the same way as before. The total number of cells in this case was 1 369 600.

The boundary condition files were also created with Gridgen. The landers'

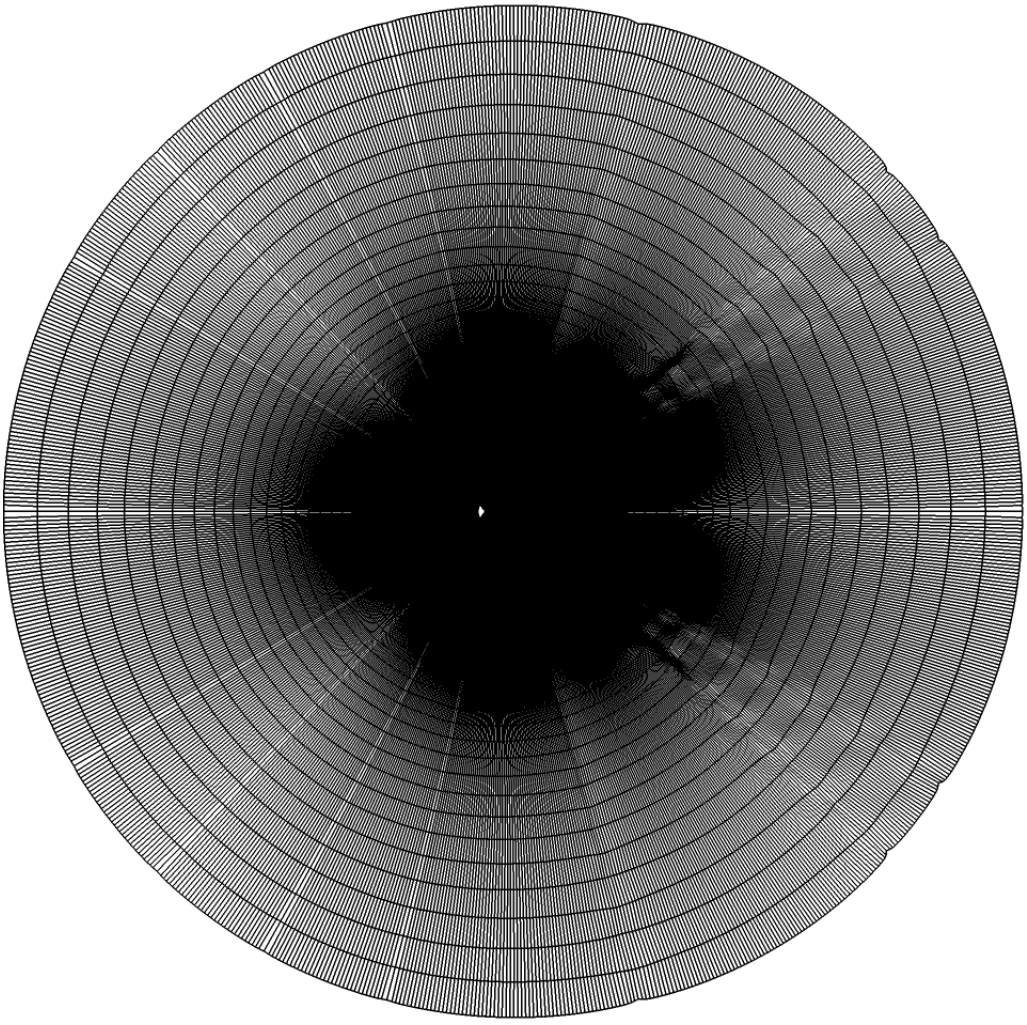

Figure 6.4: The calculation mesh created for the MIBD case.

exterior surfaces are defined as solid walls, the ends of the cell blocks get the free-stream boundary condition except for the xy-plane which gets the symmetry boundary condition.

6.1.3 The input file

The simulation parameters for FINFLO are defined in the input file. For the two geometries, a few different cases were set up to meet the variations of Reynolds and Mach numbers. All the other parameters can be held constant. See Appendix A for an example on the input file used in the simulations.

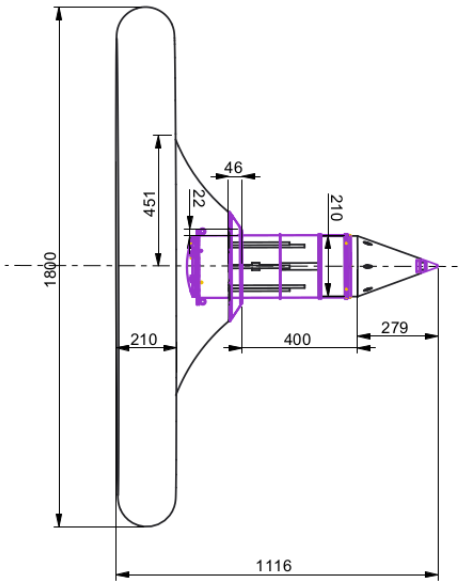

Figure 6.5: The main dimensions of the CAD model used in the creation of the AIBD case mesh.

The free stream turbulent viscosity μ_T is set to [24]

$$\mu_T = 10^{-3}\mu_\infty \tag{6.5}$$

As the free stream viscosity μ_∞ is not directly given by the user, it is solved using the parameter values that are given (Reynolds and Mach numbers, the free stream density, the speed of sound, and the reference length). The free stream turbulence level is controlled by the equation [34]

$$k_\infty < \frac{0.1U_\infty^2}{Re} \tag{6.6}$$

The Level option in the input file allows the use of coarser meshes instantly. When Level 1 is selected, the mesh (defined with the grid name file at the beginning of the input file) is used as it is. If Level is set to 2, such a grid is used where every other node is dismissed. This way, the grid has only roughly one eighth of the computation cells compared with Level 1. For this reason, it is advisable to use an odd number of nodes on all edges of the model during mesh generation. The coarsest option is Level 3. In this work, the simulations were started on Level 2 when it was possible, and then continued on Level 1 in order to have an accurate answer. This approach speeds up the calculation, since the calculation at Level 2 is much faster than at Level 1.

As noted in Section 5.1, Roe's flux splitting method was employed and full friction terms were turned off in the equations with `FULLNC = 'NO'`. This again speeds up the calculation but, in practise, does not impair the results. Additionally, this choice was recommended in the manual. Turbulence correction at walls was also turned on [35]. As for the derivative discretisation, the simulations were initiated with first-order upwind method (at Level 2) and when that was converged, the more accurate second-order upwind method was continued (at Level 1).

The Courant number is defined as

$$\mathrm{Cn} = \frac{u\Delta t}{\Delta x} \tag{6.7}$$

where u is the local velocity in a computation cell, Δt is the time step and Δx is a measure of the size of the computation cell. Even though time-averaged computation is used, it is still necessary to define a value for this number. Since implicit methods are used, it does not impose any stability limits for the simulation, and, therefore, its value can be chosen relatively freely. In practise it was noted that increasing the value increased the oscillation amplitudes at first, but the simulation converged faster. This way, choosing the right Courant number is always a compromise.

6.2 Simulations and results

6.2.1 MetNet DV with inflated MIBD

Each case with different angles of attack was simulated 5 000 iterations. The aerodynamic coefficients for the cases were then obtained by interpreting the results with the Convergence program. The program can draw graphs of the coefficients as a function of the iteration number. The values oscillate as a function of the iteration cycle, but the amplitudes diminish as the calculation progresses. This, along with the decrease of the residuals, was interpreted as the convergence of the calculation. After the mentioned 5 000 iterations, the absolute error (or: the amplitude of oscillation) of the aerodynamic coefficients had decreased to, for the majority of the cases, below ± 0.005 counts. See Figure 6.6 for an example graph and how the result was interpreted. The calculation time with the coarser grid for each case (with a fixed angle of attack) was of the order of two hours when 10 cores were used in the computer (Intel® Xeon® CPU E5-1650 v2, 3.50GHz).

Unfortunately, the maximum Mach number that was achieved in the simulations was Ma = 1.9. Even with this value, the iteration errors in the

values would grow considerably and at larger values the simulation would no longer converge. This was observed by following the growth of residuals during the simulation with the Convergence program. Thus the set of Mach numbers used for the MIBD case were Ma = 0.8, Ma = 1.3, Ma = 1.7 and Ma = 1.9.

A graph of the result for the drag coefficient can be found in Figure B.1. The conclusions that can be drawn from these results are the following:

- The effect of the Reynolds number on the drag coefficient is minimal and often within error limits. This can be seen by comparing the cases Re = 40 000 and Re = 500 000.
- The drag coefficient grows with increasing Mach number. This can be seen also in the values provided by LA, but since only four cases were simulated, it is not reasonable to calculate any approximations for the drag coefficient's evolution with the Mach number.
- While the results for large Mach numbers and small angles of attack agree well with the results from LA, there are apparent differences between the other results. The drag coefficients for subsonic speeds, calculated by FINFLO are some 10 % smaller than those obtained from the calculations by LA. It is difficult to estimate any sources for this reason due to the lack of documentation concerning the results by LA.

A graph of the result for the lift coefficient is in Figure B.2. The values are generally in fairly good agreement with the results from LA although the differences increase at the larger angles of attack. Another observation that can be made is that the lift slope C_{L_α} grows (in the sense of absolute value) as a function of the Mach number, but there is no noticeable difference between the cases Ma = 1.3 and Ma = 1.9, in which case the slope is approximately $C_{L_\alpha} \approx -0.9 \, \frac{1}{\text{rad}}$.

The most interesting result and the primary goal of this work is the set of values obtained for the pitching moment coefficient. These are drawn in Figure B.3. Even though there are, again, clear differences between the results, the tendency is clear: The slope of the pitching moment is negative. This indicates static stability for the vehicle in the simulated cases (see Section 3.2).

6.2.2 Penetrating part after the separation of the front shield (AIBD case)

Following the results from Section 4.1, three different cases were set up:

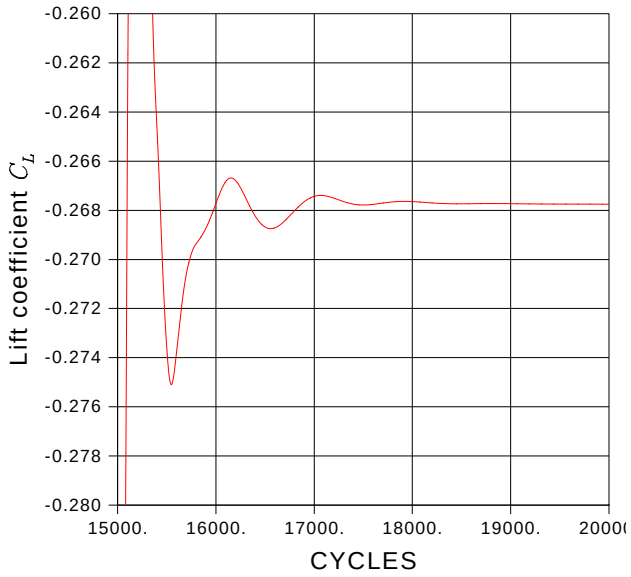

Figure 6.6: An example of plotting the lift coefficient for the MIBD case with the coarse grid. In this case, the lift coefficient can be interpreted to have the value $C_L = -0.267 \pm 0.001$. The simulation parameter values were $\alpha = 15°$, Ma = 1.3, and Re = 500 000.

- Two high Mach number cases with Ma = 0.7 and Re = 400 000 or Re = 180 000.
- A low Mach number case with Ma = 0.2 and Re = 100 000.

7 000 iterations were made for each angle of attack. After this number of iterations, the oscillations were diminished to the point that the error in the drag coefficient became ±0.02 counts and the error in the lift and pitching moment coefficients became ±0.002 counts. The results for these coefficients have been gathered in Appendix C.

The results for the lift coefficient agree well with those obtained by LA (see Figure C.2). On the other hand, the results for cases with Ma = 0.7 present about 25 % larger drag coefficients than LA. The drag coefficient at the end of the descent stage would be very close to $C_D = 1.1$, which ensures a landing speed of $U_{\text{final}} \approx 43 \ \frac{\text{m}}{\text{s}}$, see Equation (4.3).

It can also be noticed that, again, the Reynolds number has a negligible effect on the coefficients. The values of the cases with Ma = 0.7 are mostly within the error limits even though the Reynolds number is over double in the first case. A more notable change is between the two Mach numbers. The drag coefficient is roughly 20 % larger for the larger Mach number and the lift slope is roughly 20 % smaller for the larger Mach number case.

Table 6.1: The maximum values of the dimensionless wall distances, y^+, resulting from the performed simulations. For the MIBD case, the results are from the coarser grid.

	Ma	Re	max y^+
MIBD	0.8	200 000	0.3
	1.3	40 000	0.08
	1.3	500 000	0.6
	1.9	32×10^6	14
AIBD	0.2	100 000	3.4
	0.7	180 000	1.8
	0.7	400 000	1.3

The slope of the pitching moment coefficient obtained for AIBD is much smaller than the equivalent obtained by LA (see Figure C.3). They are both negative, but the source of this disparity is unknown.

6.3 Observations on grid quality

One way of assessing the grid quality is referring to the dimensionless wall distance, y^+. The goal is to keep the value relatively small, as for a small y^+, the viscous effects dominate near the wall. The values of y^+ can be obtained from the simulation results and they are gathered in Table 6.1. For the MIBD case, the results from the coarser grid are used. We can see that all cases, except for the very high Mach number case with MIBD, had a low y^+. Therefore, the approximations made in Subsection 6.1.1 were successful in most of the cases.

Looking at the results for the coefficients, the differences between the results from the coarse and the dense mesh were negligible for the lift and pitching moment coefficient. For the drag coefficient they were also relatively small. An example of this difference is in Figure 6.7.

It can be seen that numerical dissipation with the denser grid generates a higher drag coefficient for the vehicle in some cases. With the same number of iterations, the values oscillated significantly more than with the coarser grid. This was due to the numerical dissipation. Also, cases with Ma > 1.3 did not converge for the denser grid. For these reasons, the average values between the two grids are calculated in the applicable cases. These averages, as well as the direct results from the coarser grid, are tabulated in Appendix B.

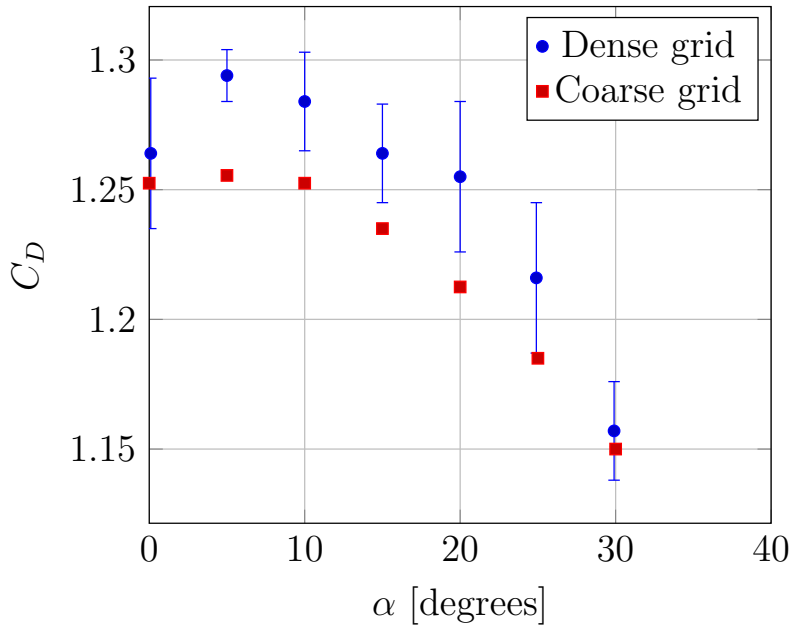

Figure 6.7: Comparison between the drag coefficient obtained with the dense grid and the coarse grid for the MIBD case. The simulation parameters were Ma = 1.3, Re = 500 000. Notice the error limits marked for the values.

6.4 Surface temperatures

A simple analysis of the surface heating, caused by friction and compressibility effects, can be done for the lander alongside the FINFLO simulations since the simulations also provide the calculated surface temperature. The goal is to obtain a rule-of-thumb for how many degrees the surface heats up as a function of the similarity parameters Re and Ma, the free stream temperature, and the angle of attack.

In this section, mainly the MIBD case is studied since it is essentially at that portion of the flight that the heat loads can be critical. The heat loads on the the AIBD case will be briefly discussed afterwards.

The shortcoming related to the maximum Mach value that was reached limits our discussion only to slightly supersonic speeds. The chemistry of the flow can change considerably at hypersonic speeds, so this review cannot predict any values at higher speeds. Since the vehicle is launched from a very high altitude, the atmosphere should be modelled with a rarified gases model. These reasons indicate that a more complete analysis of the thermal effects should be done in the future.

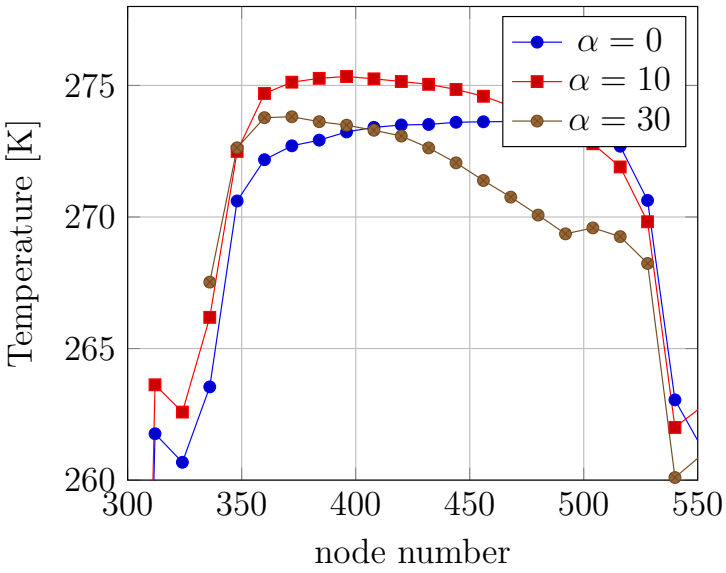

Figure 6.8: Temperatures at the frontal shield of the MIBD case with different angles of attack. $\mathrm{Ma} = 1.9$, $\mathrm{Re} = 3.2 \times 10^7$. The free stream temperature was assumed to be 170 K.

6.4.1 The effect of Angle of Attack

The way the surface temperature on the most critical part of the vehicle, the frontal thermal protection system, changes as the vehicle's angle of attack changes was studied by considering the MIBD case with $\mathrm{Ma} = 1.9$, $\mathrm{Re} = 3.2 \times 10^7$ and by taking three different angles of attack: $\alpha = 0°$, $\alpha = 10°$ and $\alpha = 30°$. The values of the wall temperatures were retrieved close to the symmetry plane (xy-plane). In this case, the values were numbered with node numbers, and node numbers of approximately 350 through 500 correspond to the frontal thermal shield.

Figure 6.8 depicts the values for the surface temperatures. The results show that as the angle of attack increases, the temperatures rise at the lower edge of the vehicle as expected. However, even at $\alpha = 30°$, the temperature change compared with the case $\alpha = 0°$ is only a few degrees. Thus the effect of angle of attack on the temperature distribution over the vehicle can be dismissed by concluding that it changes the surface temperature by only a couple of degrees.

Table 6.2: Average surface temperature on the heat shield of the MIBD case as a function of the free stream temperature. The parameter values used for the simulation were Ma = 1.3, Re = 500 000 and $\alpha = 35°$.

Free stream temperature T_∞ [K]	Average frontal surface temperature T [K]	T/T_∞
140	183.62	1.31
160	205.95	1.29
180	231.48	1.29
200	255.27	1.28
220	281.27	1.28

6.4.2 The effect of free stream temperature

Similarly as in the previous subsection, the temperature of the thermal protection system was studied as a function of the free stream temperature. This time, the MIBD case with Ma = 1.3, Re = 500 000 and $\alpha = 35°$ was studied. The range of the free stream temperatures was chosen to match the values that the vehicle might experience during the descent phase (see Figure 2.4). The average values of wall temperatures corresponding to the frontal heat shield were calculated for each case and the results are in Table 6.2.

The regression for the values shows that an increase of 10 K in the free stream temperature raises the surface temperature by approximately 12.2 K. This cannot, however, fully predict the surface temperatures since it is also dependent of other parameters. Nevertheless, this is a useful value that can be used to estimate changes in the temperature.

6.4.3 The effect of the Reynolds number

For the case of the MIBD configuration at Ma = 1.3, two different cases with largely different Reynolds numbers were calculated earlier. The surface temperatures can now be compared in order to assess the effect of the Reynolds number in this case. Statistics of the wall temperatures have been gathered in Table 6.3. The points were again gathered to correspond to the most critical part of the vehicle, nodes 350 through 500. As can be easily seen, the difference in the mean temperature is very small. Also, a simple two-mean Z-test gives a p-value of $p \approx 0.215$, confirming that the two means are not significantly different. Thus it can be concluded that the Reynolds number has virtually no effect on the surface temperature.

Table 6.3: Average surface temperature on the heat shield of the MIBD case with two different Reynolds numbers. Parameter values Ma = 1.3 and $\alpha = 35°$ were used and the free stream temperature was set to 170 K.

	Re = 40 000	Re = 500 000
Average temperature, K	218.585	218.663
Standard deviation, K	0.876	0.844
Number of points	150	150

6.4.4 The effect the Mach number

Effects of the Mach number can be studied in a similar fashion with the previous subsection. As it was seen that the Reynolds number has virtually no effect on the surface temperature, we can let it vary as was done in the simulations earlier. The cases to be compared are Ma = 0.8 with Re = 200 000 and Ma = 1.3 with Re = 500 000. The thermal images of the lander can be seen in Figure 6.9.

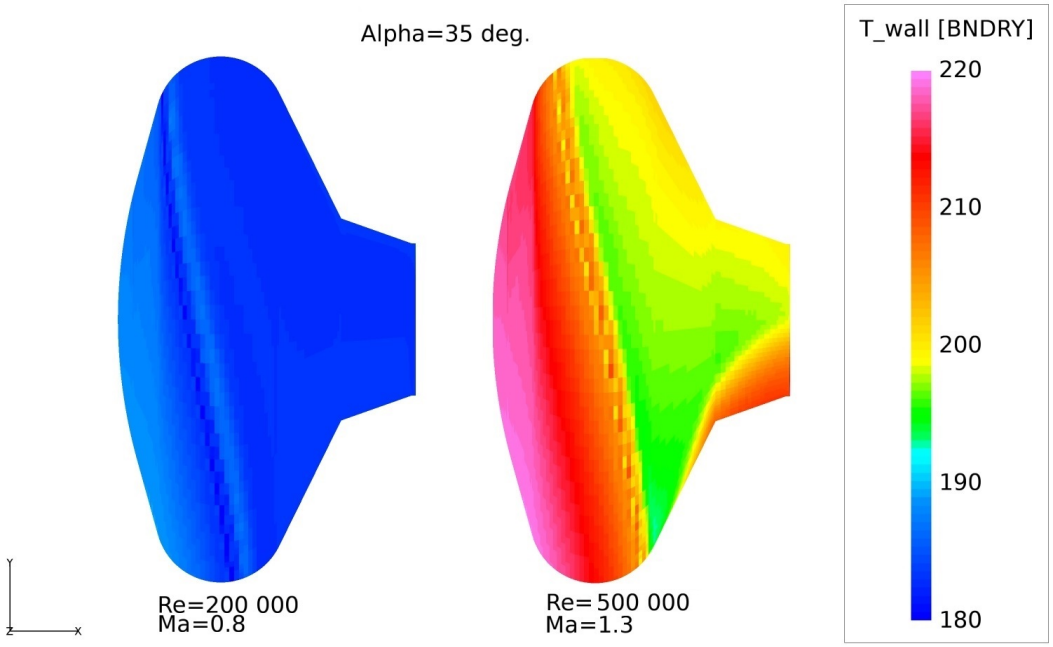

Figure 6.9: Temperatures around the MIBD case with two different Mach numbers. The free stream temperature was chosen to be 170 K.

The average temperature on the thermal shield was 188.4 K for Ma = 0.8 and 218.6 K for Ma = 1.3. The difference, about 30 K, is indeed significant. Unfortunately, as no results were obtained at Mach numbers larger

than Ma = 1.9, it is not possible to use these values to predict the surface temperatures at greater Mach numbers. It is only possible to conclude that at subsonic speeds the thermal effects are not very large and the vehicle heats up perhaps some order of 10 K during this portion of flight. On the other hand, the high supersonic speeds do generate considerable heat loads on the vehicle.

6.4.5 Heat loads on AIBD

Since the largest heat loads appear when the Mach number is the largest, it is sensible to take a look at the AIBD case at Ma = 0.8. Figure 6.10 portrays the heat distribution around the vehicle.The calculation shows that, surprisingly, the warmest regions in this case would be on the backside of the vehicle, where the surface temperature can reach even 30 K warmer temperatures than the front face and 50 K warmer than the free stream temperature. It is possible that in reality the result is quite different, since the structure was modeled as solid in these simulations.

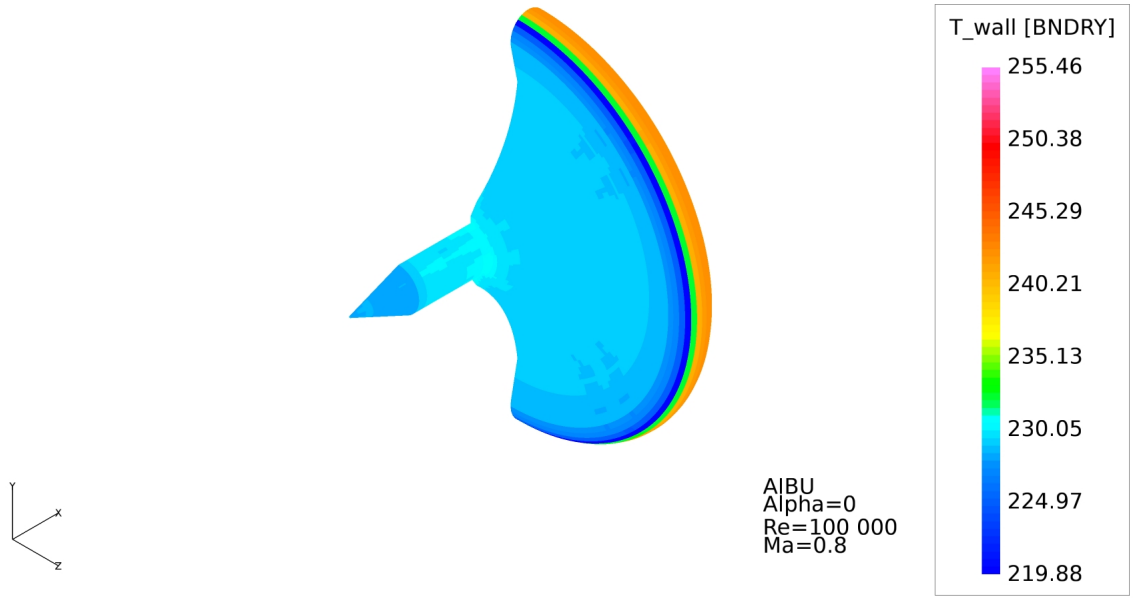

Figure 6.10: Temperatures around the AIBD case. The free stream temperature was set to 207 K.

Chapter 7

Conclusions and discussion

In this thesis, the aerodynamics of the Mars MetNet descent vehicle was analysed by using the CFD software FINFLO by Aalto University. The MetNet EDLS has been developed in cooperation by the team comprising FMI, LA, and Instituto Nacional de Técnica Aeroespacial with the responsibility of aerodynamic design resting with LA. The simulations were set up to match the re-entry and descent conditions on Mars as closely as possible. In order to facilitate the parameter selection, an atmospheric model was created in order to approximately calculate the averages of temperature, density, the speed of sound, the specific heat ratio, and the dynamic viscosity as a function of altitude. The main source for these values was the Mars Climate Database.

A trajectory calculation code in Python was also developed with the explicit first-order forward Euler method in order to calculate the combination of Reynolds and Mach numbers that the vehicle experiences during the descent phase. The trajectory calculations provided a condition for the dimensionless wall distance y^+ of the calculation mesh and therefore also helped in the mesh generation. Two major MetNet geometries during the atmospheric entry trajectory, MIBD for the entry phase and AIBD for the descent phase, were modelled and simulated. Additionally, two different meshes were generated for the former in order to assess the quality of the mesh.

The main goal of this work was to obtain the pertinent aerodynamic coefficients and, therefore, to reinforce the results obtained by LA. The most interesting aerodynamic feature of the vehicle is the pitching moment coefficient C_m, a dimensionless measure of the tendency of the vehicle to rotate around its centre of mass as a response to aerodynamic effects. Studying the values of this coefficient is essential in the analysis of the stability of the vehicle, since the slope of the pitching moment coefficient with respect to the angle of attack (see Section 3.1) determines the static stability of the vehicle. Dynamic stability, on the other hand, can be studied by calculating the slope

of this coefficient with respect to the pitch rate. Only the former of these two is studied in this work due to extensive computations required by the latter.

The drag coefficient C_D, a measure of the air resistance generated by the flow around the vehicle, is another important quantity in the aerodynamic analysis of the lander. It enables the computation of the deceleration during the re-entry and descent phase. The final impact speed is a function of the drag coefficient and a large enough value is desired in order to ensure a safe landing for the vehicle. The drag coefficient, along with the other pertinent aerodynamic coefficients, is calculated with the FINFLO simulations in this work and then compared with the results by LA. The simulations also provide some insight to the temperature distributions around the vehicle and how it evolves as a function of different parameters.

The main contributions of this work are the atmospheric model, where the regressions are presented as equations that can be used later, the trajectory code and the aerodynamic coefficients of the vehicle as a function of the angle of attack. These are the necessary tools in the aerodynamic analysis of the vehicle in its re-entry and descent phase. The results can be used in future calculations that could include heat transfer analyses or dynamic (time-dependent) CFD simulations.

A major conclusion can be drawn from aerodynamic analysis using FINFLO simulations is that the MetNet Lander is statically stable at least up to Mach number 1.9. This result includes two points of caution. Firstly, the result only encompasses the feature of static stability and not yet dynamic stability. On the other hand, the aerodynamic simulations and wind tunnel tests performed by Lavochkin Association indicate that the MetNet landing vehicle would be also dynamically stable during the entry and descent phase. Secondly, the limitations of the code permitted converging simulations only up to the mentioned Mach number. The slope of the pitching moment coefficient was negative for all these simulations, which is a promising result, but it is difficult to estimate how this value would evolve at hypersonic speeds. The earlier simulations by LA show strong nonlinear behaviour of C_m for higher speeds, and hence proper simulations with higher Mach numbers should be carried out. A specialised rarified gases code or a hypersonic model with a refined gas chemistry model should be used for such simulations.

The numerical values of the lift coefficient are in fairly good agreement with the earlier results by the LA, especially during the AIBD phase. This aspect serves as evidence for the validity of the results. On the other hand, other aerodynamic coefficients exhibit more deviations with the earlier analyses. For example, our results for the drag coefficient present noticeable differences between LA's results almost across the board. However, the change

is in a positive direction, as a large drag coefficient is specifically desired.

Finally, the thermal results point out that the most drastic heating of the vehicle develops at supersonic speeds as expected. For this reason, mainly the MIBD state is subject to heating. The parameters determining the surface temperature are shown to be the Mach number and the free stream temperature, while the Reynolds number and the angle of attack (assuming that they stay within certain limits) have a practically negligible effect.

The analyses of this thesis suggest that the Mars MetNet vehicle is statically stable during the entry and descent trajectory phases during its landing on Mars through the Martian atmosphere. The conclusions are similar to those gained by the earlier work by the MetNet development team. The modelling and simulations included various simplifications and idealisations that should be taken into account when making MetNet system and missions decisions. Additional modelling and simulation work are recommended to confirm the thesis results. Furthermore, additional aerodynamic simulations and wind tunnel tests will facilitate the extension of the thesis results such that they will contribute to the dynamic stability analysis of the MetNet vehicle.

Bibliography

[1] NASA & California Institute of Technology, "Mars exploration rovers," http://mars.nasa.gov/mer/mission/spacecraft_edl.html. Retrieved February 2nd, 2015.

[2] NASA & California Institute of Technology, "Mars exploration rover," http://www.jpl.nasa.gov/news/fact_sheets/mars03rovers.pdf. Retrieved February 3rd, 2015.

[3] Finnish Meteorological Institute, "Mars MetNet Mission," http://metnet.fmi.fi/index.php. Retrieved February 3rd, 2015.

[4] A.-M. Harri, "RITD final report," technical report, February 24th 2015.

[5] Russian Aviation and Space Agency, "Project documentation for selected concept," technical report, April 17th 2002.

[6] A-M. Harri, S. Alexashin et al., "Mars MetNet Mission Status," http://www.researchgate.net/publication/282274917_Mars_MetNet_Mission_Status. Retrieved October 5th 2015.

[7] A. Hellsten, K. Kaarlonen, J. Saloranta et al., "Finflo-flow solver." http://www.aero.hut.fi/Englanniksi/CFD_text/finflo__flow_solver.html. Retrieved February 3rd, 2015.

[8] Finnish Meteorological Institute, "Mars MetNet Mission," http://metnet.fmi.fi/index.php?id=93. Retrieved February 17th, 2015.

[9] A-M. Harri, P. Makkonen et al., "Martian Atmospheric Science Network - MetNet," https://iafastro.directory/iac/archive/browse/IAC-04/IAA.3.7/2/815/. Retrieved October 9th 2015.

[10] Lavochkin Association, "Scaling laws for Mars - Earth Re-entry System," technical report, December 24th 2012.

[11] Lavochkin Association, "Mathematical Model for projecting the wind tunnel test results for Earth's atmosphere," technical report, December 20th 2012.

[12] Lavochkin Association, "Test plan for the wind tunnel tests," technical report, December 27th 2013.

[13] Lavochkin Association, "Test report of the wind tunnel tests," technical report, July 28th 2014.

[14] Lavochkin Association, "Feasibility and design of EDLS system for Earth's atmosphere," technical report, December 27th 2014.

[15] Lavochkin Association, "Analysis of an inflatable EDLS' dynamic stability in the transsonic regime," technical report, September 12th 2012.

[16] LMD, OU, IAA, ESA, CNES, "Mars Climate Database: The Web Interface," http://www-mars.lmd.jussieu.fr/mcd_python/. Retrieved March 6th 2015.

[17] F. Forget, E. Millour, and S. Lewis, "Mars Climate Database v5.1 Detailed Design Document," http://www-mars.lmd.jussieu.fr/mars/info_web/MCD5.1_ddd.pdf. Retrieved March 3rd 2015.

[18] C. Justus, A. Duvall, and V. Keller, "Validation of Mars Global Reference Atmospheric Model (Mars-GRAM 2001) and planned new features," http://www.sciencedirect.com/science/article/pii/S0273117706004510. Retrieved March 9th 2015.

[19] A. Miettinen, E. Salminen, and T. Siikonen, "Kaksifaasivirtaussimulointimenetelmien kehitystä ja sovelluksia - Raportti 10," Finflo Oy. Espoo 2003.

[20] Lavochkin Association, "Feasibility of MetNet EDLS to Earth Reentry," technical report, December 27th 2011.

[21] Wikipedia, "Knudsen number," https://en.wikipedia.org/wiki/Knudsen_number. Retrieved July 16th 2015.

[22] Lavochkin Association, "Small (mini) landing station system tests," technical report, December 10th 2012.

[23] Lavochkin Association, "Manufacturing of the MML's experimental models and ground-based test schedule," technical report, July 27th 2004.

[24] Finflo Ltd., *FINFLO User Guide - Version 8.1.* Espoo 2003.

[25] D. F. Kurtulus, F. Scarano, and L. David, "Unsteady aerodynamic forces estimation on a square cylinder by TR-PIV," *Springer*, 2006.

[26] J. Roskam, *Airplane Flight Dynamics and Automatic Flight Controls – Part I.* 2011. ISBN-13 978-1-884885-17-4.

[27] J. Adams, "Atmospheric re-entry," *Exoaviation, nd Web.* *http://exoaviation.webs.com/pdf_files/AtmosphericRe-Entry.pdf*, 2003.

[28] D. Wilcox, *Turbulence Modeling for CFD.* 1993. ISBN-0-9636051-0-0.

[29] F.R Menter, "Two-Equation Eddy Viscosity Turbulence Models for Engineering Applications," 1994. AIAA Journal, Vol. 32, No.8.

[30] A. Hellsten, "Some Improvements in Menter's k-ω SST turbulence model," http://cfd.mace.manchester.ac.uk/twiki/pub/Main/CDAdapcoMeetingsM4/AIAA_98-2554-CP.PS.pdf. Retrieved October 16th 2015.

[31] L. Vienne, "CFD Simulation of a Re-Entry Mars Vehicle," report, August 7th 2015.

[32] F. White, "Fluid Mechanics, Third Ed.," 2004. ISBN 0-07-11376-3. McGraw-Hill,Inc.

[33] Pointwise, "Gridgen," http://www.pointwise.com/gridgen/. Retrieved October 16th 2015.

[34] NASA Langley Research Center, "The Menter Shear Stress Transport Turbulence Model," http://turbmodels.larc.nasa.gov/sst.html. Retrieved October 30th 2015.

[35] P. Rautaheimo and T. Siikonen, "Improved Solid-Wall Boundary Treatment in Low-Reynolds-Number Turbulence Models," AIAA Journal, May 2001.

Appendix A

Input File Example

```
&WORKS
  IOLD1  = 1                          # Iteration control
  GRIDFI = 'MIBU-Block-volumes.grd' # Grid file name
  BCFILE = 'MIBU-August-bc-FINFLO.BC' # Boundary condition file name
&END

&INPUTS
  NAME    = 'MetNet Lander'         # Name of the simulation
  KSCAL   = 0                       # Number of scalar equations
  ISTRES  = 0                       # Reynolds stress-relation parameter
  FLUXTY  = 'roe'                   # Flux splitting method
  FULLNC  = 'NO'                    # Full friction term
  CFL     = 3.0                     # Courant number
  ICMAX   = 145000                  # Maximum number of iterations
  IPRESC  = 0                       # Compressible simulation
  TIMEC   = 'NO'                    # Time accurate calculation
  DT      = 0.1                     # Time step in time accurate
                                    # calculation
  TMAX    = 4.0                     # End time in time accurate calculation
  LEVEL   = 1                       # Calculation level
  FRSTEM  = 170.0                   # Free stream temperature
  TEMINI  = 170.0                   # Initial temperature
  AREF    = 0.403771                # Reference area
  GRILEN  = 1.0E-3                  # Grid scaling factor
  CHLREF  = 1.014                   # Reference length
  RE      = 3.2E+7                  # Reynolds number
  RMACH   = 1.9                     # Mach number
  ITURB   = 6                       # Turbulence model (6 -> SST k-omega)
```

```
  KP      = 5000        # Interval for updating the output file
  ALPHA   = 30.0        # Angle of attack
  ISTATE  = 1           # Gas state equation (1 -> perfect gas)
  IDRXX   = 6           # Variable written in the history as maximum change
  XMOM    = 0.314       # Moment reference point location, x-coordinate
  YMOM    = 0.0         # Moment reference point location, y-coordinate
  TURCOC  = 'yes'       # Turbulence correction at walls
  XXTRAC  = 'no'        # Distance weighted interpolation
  TRUE_DISTC = 'YES'    # Accurate wall distance calculation
      STATEC = 'NO'     # Use standard values for Sutherland coefficients
      RGAS   = 190.     # The specific gas constant
      GAMMA  = 1.35     # Specific heat ratio
      VISU0  = 1.92E-7  # Sutherland coefficient
      EXPSU  = 1.8      # Sutherland coefficient
      TSU0   = 60.      # Sutherland coefficient
&END

&BLOCKS
  INIT(:) = 10*1        # Initial condition type
  MGRID(:)= 10*2        # Number of multigrid levels
  IDER(:) = 10*2        # Derivatives calculated by Gauss approach
  INTERI(:) = 10*+1     # Derivative discretization type in I-direction
  INTERJ(:) = 10*-1     # Derivative discretization type in J-direction
  INTERK(:) = 10*-1     # Derivative discretization type in K-direction
  LAMIN(:)= 10*111      # Laminar approximation direction
  OMEGA(:)   = 10*0.0   # Angular speed
  SOLUTION_TYPE(:) ='FLUID'
  FRSMUTB(:) = 10*0.0   # Minimum dissipation of turbulent kinetic energy
  FRSTURB(:) = 10*0.0   # Free stream turbulence level
  TURLIMB(:) = 10*15000.# Maximum dimensionless turbulent viscosity
  IK(:) = 1             # Output slab level
  IL(:) = 3             # Direction of output slab
  IT(:) = 100           # First index in output slab
  MOV(:) = 0            # Movie creation (0 -> no)
&END
&FLIGHT
&END

&FORCE_GROUP_DATA
&END
```

Appendix B

Aerydynamic coefficients of the MIBD case

Table B.1: The drag coefficient of the MIBD case, calculated with FINFLO. The error limits come from the oscillation limits of the coefficients. Thus the values should be interpreted as "Average" ± "Error". N/A means that the results were not available.

C_D										
Ma	0.8		1.3		1.3		1.7		1.9	
Re	200 000		40 000		500 000		32×10^6		32×10^6	
α	Average	Error	Average	Error	Average	Error	Average	Error	Average	Error
0	0.863	0.003	1.260	0.002	1.253	0.002	1.240	0.045	1.280	0.005
5	0.863	0.003	1.261	0.001	1.256	0.002	1.238	0.033	1.283	0.003
10	0.850	0.005	1.255	0.001	1.253	0.002	1.233	0.003	1.275	0.005
15	0.830	0.005	1.238	0.002	1.235	0.005	1.218	0.002	1.260	0.060
20	0.803	0.003	1.213	0.003	1.213	0.003	1.200	0.050	1.230	0.010
25	0.763	0.003	1.183	0.003	1.185	0.005	1.180	0.010	1.205	0.035
30	0.718	0.003	1.143	0.002	1.150	0.002	1.155	0.005	1.165	0.005
35	0.663	0.003	1.099	0.001	1.108	0.003	1.120	0.020	N/A	N/A

Table B.2: The lift coefficient of the MIBD case, calculated with FINFLO.

C_L										
Ma	0.8		1.3		1.3		1.7		1.9	
Re	200 000		40 000		500 000		32×10^6		32×10^6	
α	Average	Error	Average	Error	Average	Error	Average	Error	Average	Error
0	0.0	0.0010	0.0	0.0010	0.0	0.0010	0.0	0.0020	0.0	0.0020
5	-0.0725	0.0025	-0.0900	0.0020	-0.0910	0.0010	-0.0875	0.0125	-0.1000	0.0100
10	-0.1400	0.0050	-0.1790	0.0010	-0.1810	0.0010	-0.1775	0.0025	-0.1800	0.0100
15	-0.2040	0.0020	-0.2640	0.0020	-0.2670	0.0010	-0.2575	0.0025	-0.2600	0.0200
20	-0.2625	0.0025	-0.3460	0.0020	-0.3510	0.0010	-0.3400	0.0200	-0.3450	0.0050
25	-0.3125	0.0025	-0.4225	0.0025	-0.4290	0.0010	-0.4125	0.0025	-0.4250	0.0150
30	-0.3525	0.0025	-0.4900	0.0050	-0.5010	0.0010	-0.4875	0.0025	-0.4900	0.0100
35	-0.3800	0.0050	-0.5500	0.0100	-0.5650	0.0010	-0.5450	0.0150	N/A	N/A

Table B.3: The pitching moment coefficient about the centre of mass of the MIBD case, calculated with FINFLO.

C_m										
Ma	0.8		1.3		1.3		1.7		1.9	
Re	200 000		40 000		500 000		32×10^6		32×10^6	
α	Average	Error	Average	Error	Average	Error	Average	Error	Average	Error
0	0.0	0.0001	0.0	0.0002	0.0	0.0002	0.0	0.0010	0.0	0.0004
5	-0.0143	0.0003	-0.0113	0.0003	-0.0121	0.0001	-0.0120	0.0040	-0.0145	0.0015
10	-0.0283	0.0003	-0.0223	0.0003	-0.0239	0.0001	-0.0245	0.0005	-0.0220	0.0010
15	-0.0415	0.0005	-0.0328	0.0003	-0.0349	0.0001	-0.0325	0.0005	-0.0310	0.0070
20	-0.0538	0.0002	-0.0423	0.0003	-0.0448	0.0002	-0.0400	0.0040	-0.0385	0.0005
25	-0.0653	0.0003	-0.0503	0.0003	-0.0532	0.0001	-0.0473	0.0003	-0.0450	0.0030
30	-0.0753	0.0003	-0.0565	0.0005	-0.0597	0.0001	-0.0533	0.0003	-0.0510	0.0030
35	-0.0843	0.0003	-0.0608	0.0002	-0.0648	0.0002	-0.0600	0.0020	N/A	N/A

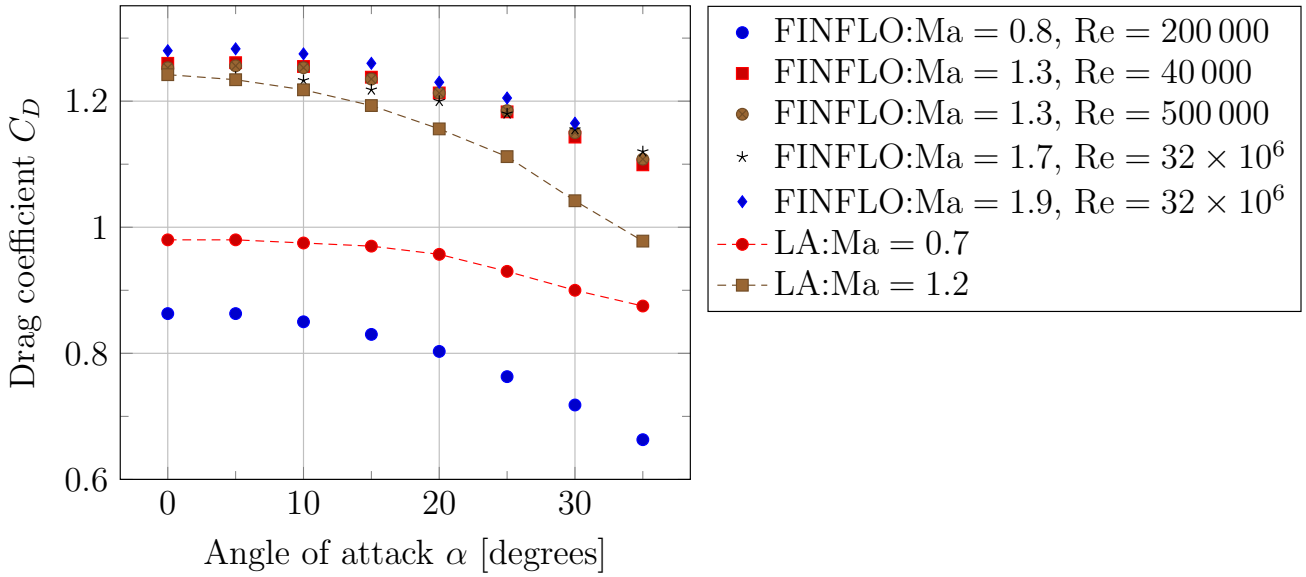

Figure B.1: Comparison between the drag coefficients for the MIBD case obtained by the FINFLO simulations and from LA. Note that conversion using Eq. (2.15) was used for LA's results in order to enable the comparison.

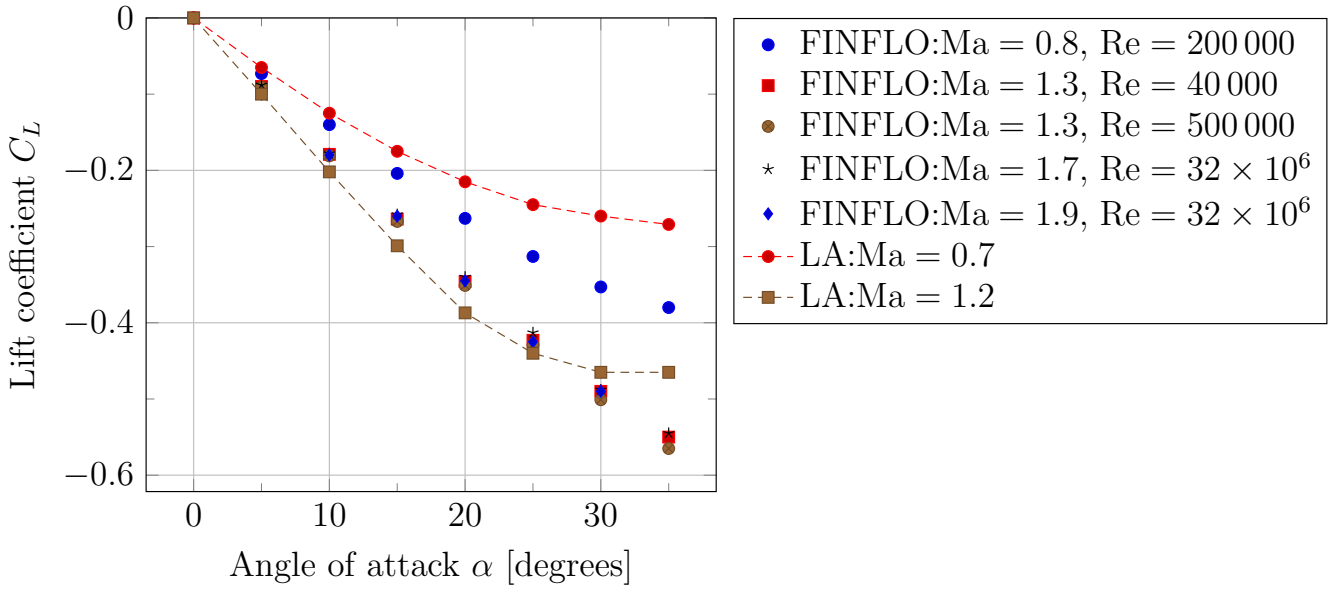

Figure B.2: Comparison between the lift coefficients for the MIBD case obtained by the FINFLO simulations and from LA.

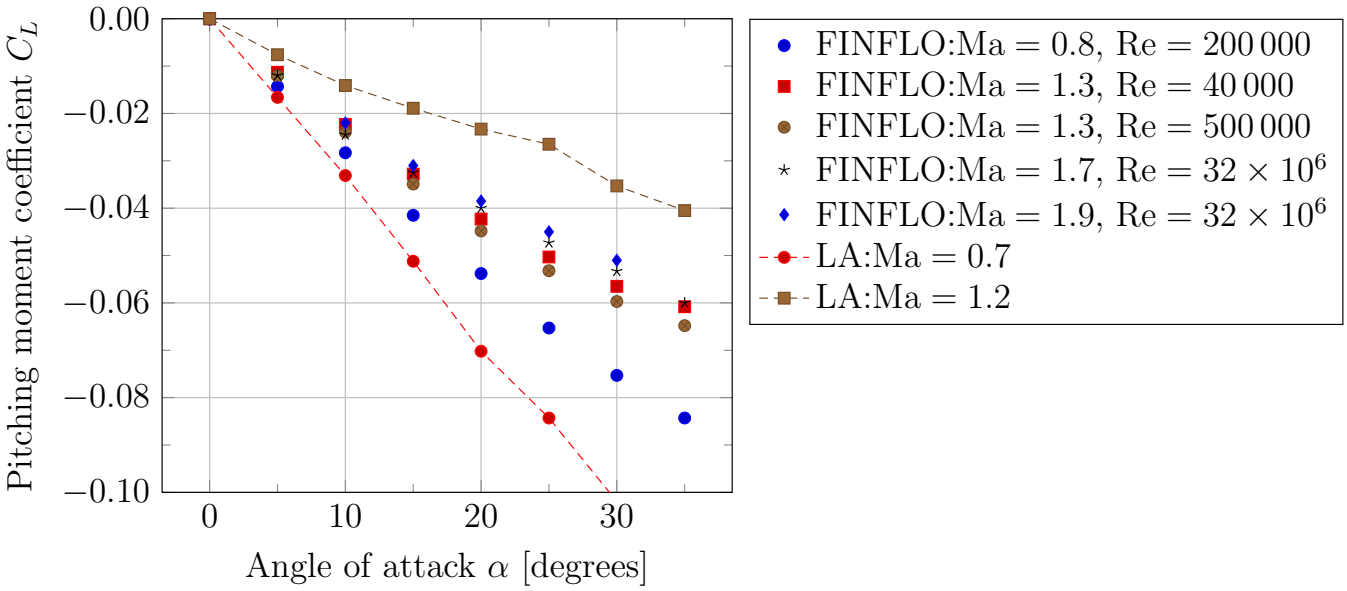

Figure B.3: Comparison between the pitching moment coefficients for the MIBD case obtained by the FINFLO simulations and from LA. Note that the conversion of the reference point using Eq. (2.16) was used for LA's results in order to enable the comparison.

Table B.4: Comparison between the drag coefficients of MIBD obtained with the coarse and the dense mesh. The average value is the arithmetic mean of the two values. The error is ±0.045 counts.

C_D									
Ma	1.3			1.3			0.8		
Re	500 000			40 000			200 000		
α	Coarse	Dense	Average	Coarse	Dense	Average	Coarse	Dense	Average
0	1.253	1.264	1.258	1.260	1.284	1.272	0.863	0.934	0.898
5	1.256	1.294	1.275	1.261	1.313	1.287	0.863	0.924	0.893
10	1.253	1.284	1.268	1.255	1.298	1.277	0.850	0.924	0.887
15	1.235	1.264	1.250	1.238	1.269	1.253	0.830	0.885	0.858
20	1.213	1.255	1.234	1.213	1.240	1.226	0.803	0.866	0.834
25	1.185	1.216	1.200	1.183	1.191	1.187	0.763	0.807	0.785
30	1.150	1.157	1.154	1.143	1.162	1.152	0.718	0.768	0.743

Table B.5: Comparison between the lift coefficients of MIBD obtained with the coarse and the dense mesh. The error is ±0.01 counts.

C_L									
Ma	1.3			1.3			0.8		
Re	500 000			40 000			200 000		
α	Coarse	Dense	Average	Coarse	Dense	Average	Coarse	Dense	Average
0	0	0	0	0	0	0	0	0	0
5	-0.091	-0.097	-0.094	-0.091	-0.097	-0.094	-0.073	-0.068	-0.070
10	-0.181	-0.195	-0.188	-0.181	-0.195	-0.188	-0.140	-0.141	-0.141
15	-0.267	-0.282	-0.275	-0.267	-0.282	-0.275	-0.204	-0.209	-0.207
20	-0.351	-0.360	-0.355	-0.351	-0.360	-0.355	-0.263	-0.267	-0.265
25	-0.429	-0.438	-0.433	-0.429	-0.438	-0.433	-0.313	-0.316	-0.314
30	-0.501	-0.511	-0.506	-0.501	-0.511	-0.506	-0.353	-0.355	-0.354

Table B.6: Comparison between the pitching moment coefficients of MIBD obtained with the coarse and the dense mesh. The pitching moment was calculated around the centre of mass. The error is ±0.003 counts.

C_m									
Ma	1.3			1.3			0.8		
Re	500 000			40 000			200 000		
α	Coarse	Dense	Average	Coarse	Dense	Average	Coarse	Dense	Average
0	0	0	0	0	0	0	0	0	0
5	-0.012	-0.023	-0.017	-0.012	-0.023	-0.017	-0.014	-0.021	-0.017
10	-0.024	-0.036	-0.030	-0.024	-0.036	-0.030	-0.028	-0.034	-0.031
15	-0.035	-0.048	-0.041	-0.035	-0.048	-0.041	-0.042	-0.047	-0.044
20	-0.045	-0.059	-0.052	-0.045	-0.059	-0.052	-0.054	-0.059	-0.056
25	-0.053	-0.068	-0.061	-0.053	-0.068	-0.061	-0.065	-0.069	-0.067
30	-0.060	-0.076	-0.068	-0.060	-0.076	-0.068	-0.075	-0.079	-0.077

Appendix C

Aerodynamic coefficients of the AIBD case

Table C.1: The drag coefficient of the AIBD case, calculated with FINFLO. The error limits come from the oscillation limits of the coefficients. Thus the values should be interpreted as "Average" ± "Error".

C_D						
Ma	0.2		0.7		0.7	
Re	100 000		180 000		400 000	
α	Average	Error	Average	Error	Average	Error
0	1.099	0.012	1.3457	0.0123	1.333	0.012
5	1.123	0.012	1.3642	0.0062	1.327	0.031
10	1.099	0.012	1.3395	0.0062	1.327	0.031
15	1.074	0.012	1.3025	0.0062	1.265	0.031
20	1.025	0.012	1.2407	0.0062	1.222	0.012
25	0.951	0.012	1.1728	0.0123	1.160	0.012
30	0.877	0.012	1.0926	0.0062	1.074	0.012
30	0.802	0.012	0.9938	0.0062	0.975	0.012

Table C.2: The lift coefficient of the AIBD case, calculated with FINFLO.

C_L						
Ma	0.2		0.7		0.7	
Re	100 000		180 000		400 000	
α	Average	Error	Average	Error	Average	Error
0	0.0	0.001	0.0	0.0012	0.0	0.002
5	-0.090	0.003	-0.1080	0.0006	-0.107	0.001
10	-0.182	0.003	-0.2191	0.0031	-0.219	0.001
15	-0.262	0.003	-0.3247	0.0012	-0.323	0.002
20	-0.336	0.003	-0.4160	0.0012	-0.414	0.002
25	-0.398	0.003	-0.4963	0.0025	-0.494	0.005
30	-0.448	0.003	-0.5617	0.0062	-0.556	0.006
30	-0.485	0.003	-0.6080	0.0031	-0.602	0.003

Table C.3: The pitching moment coefficient about the centre of mass of the AIBD case, calculated with FINFLO.

C_m						
Ma	0.2		0.7		0.7	
Re	100 000		180 000		400 000	
α	Average	Error	Average	Error	Average	Error
0	0.0	0.0014	0.0	0.0014	0.0	0.0014
5	-0.0233	0.0014	-0.0213	0.0007	-0.0213	0.0007
10	-0.0453	0.0014	-0.0391	0.0007	-0.0391	0.0007
15	-0.0672	0.0014	-0.0556	0.0007	-0.0569	0.0007
20	-0.0864	0.0014	-0.0720	0.0007	-0.0741	0.0014
25	-0.1049	0.0007	-0.0885	0.0007	-0.0898	0.0007
30	-0.1221	0.0014	-0.1022	0.0007	-0.1049	0.0007
30	-0.1385	0.0014	-0.1159	0.0007	-0.1187	0.0007

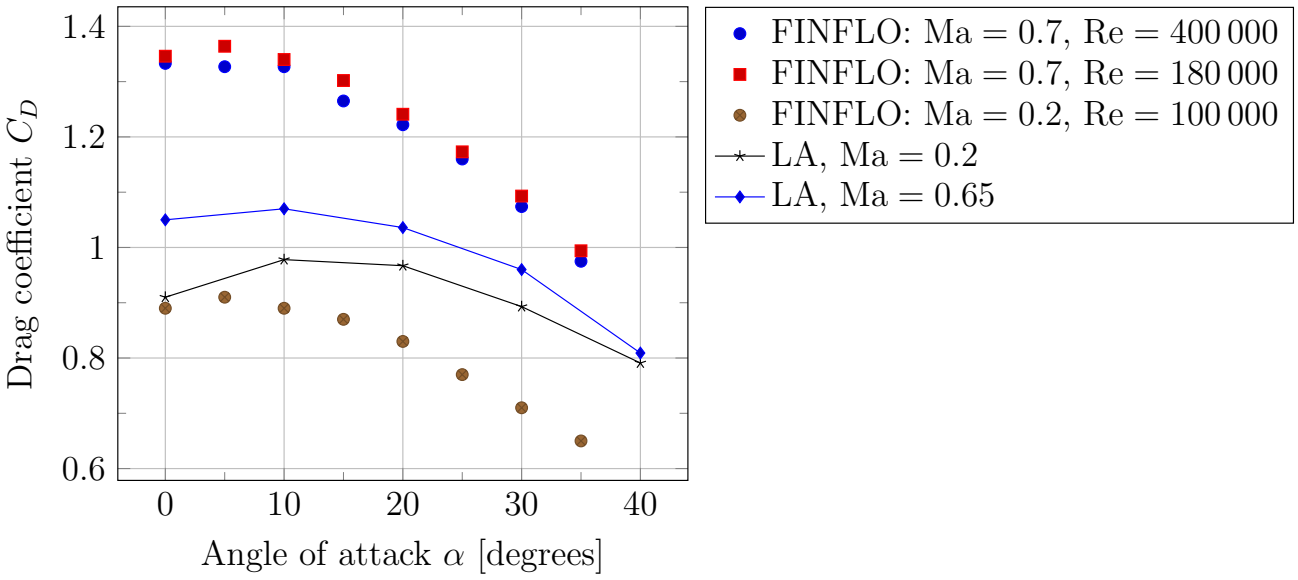

Figure C.1: Comparison between the drag coefficients obtained with FINFLO simulations and from LA for the AIBD case.

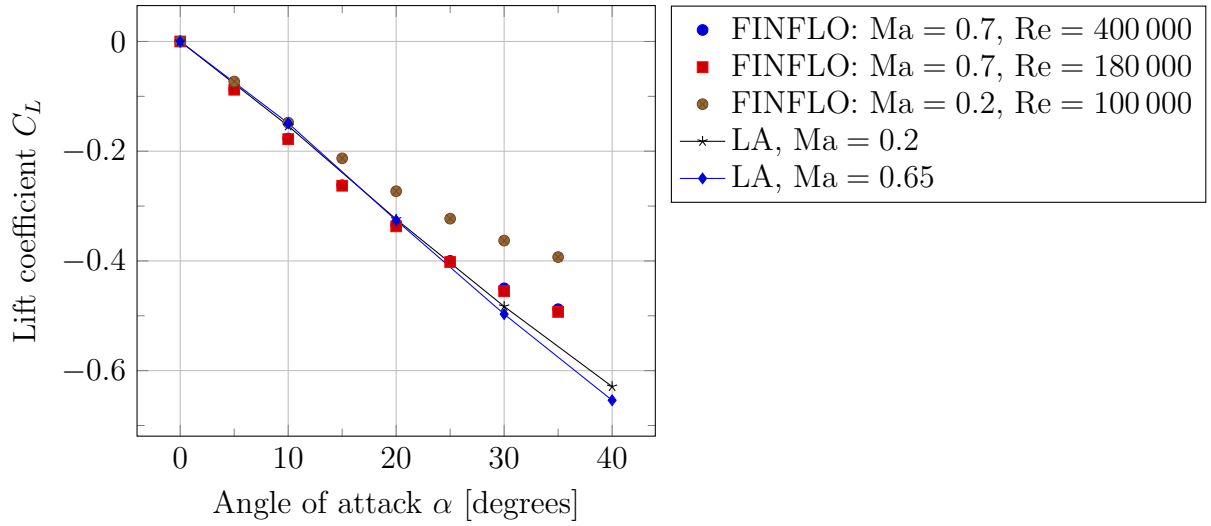

Figure C.2: Comparison between the lift coefficients obtained with FINFLO simulations and from LA for the AIBD case.

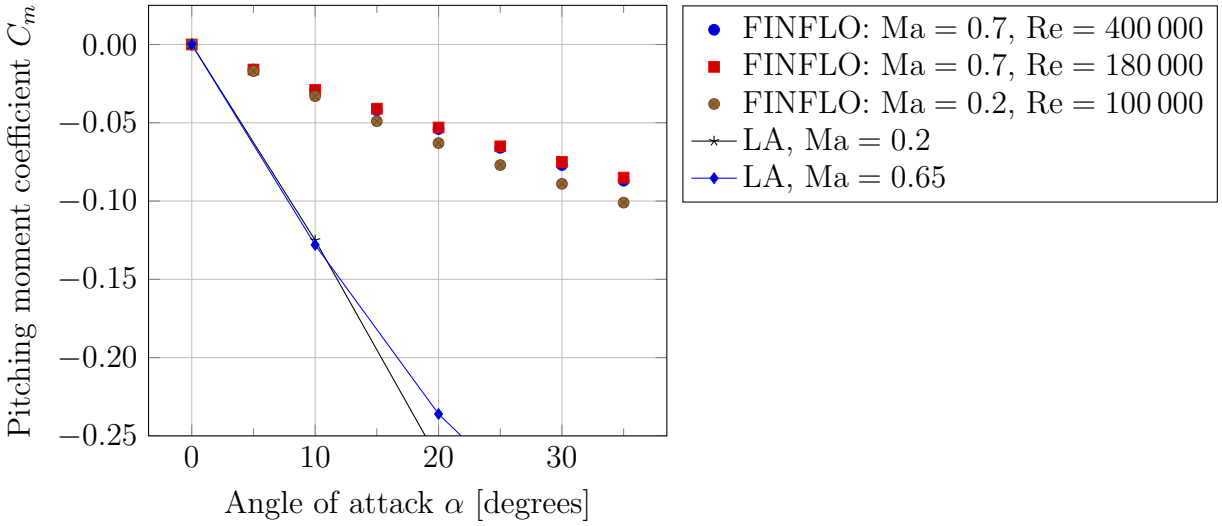

Figure C.3: Comparison between the pitching moment coefficients obtained with FINFLO simulations and from LA for the AIBD case. The results from LA were converted using Equation (2.16) to correspond to the same reference point as what was used in the FINFLO simulations, that is the centre of mass.